JGR Solid Earth

RESEARCH ARTICLE
10.1029/2019JB019029

Seismic Anisotropy and Its Impact on Imaging the Shallow Alpine Fault: An Experimental and Modeling Perspective

Ludmila Adam[1], Marcel Frehner[2], Katrina Sauer[3], Virginia Toy[3,4], and Simon Guerin-Marthe[5]

[1]School of Environment, University of Auckland, Auckland, New Zealand, [2]Department of Earth Sciences, ETH Zürich, Zürich, Switzerland, [3]Department of Geology, University of Otago, Dunedin, New Zealand, [4]Institut für Geowissenschaften Johannes Gutenberg Universität-Mainz, Mainz, Germany, [5]Department of Earth Sciences, Durham University, Durham, UK

Key Points:
- By combining elastic wave models and laboratory data of Alpine Fault protomylonites, we show the effects of mineral anisotropy and fractures
- Microstructures imaging and numerical modeling confirm open grain boundaries and (micro) fractures at all depths within the brittle regime
- These combined structural features explain field observations of high seismic reflectivity and low velocities within the Alpine Fault

Supporting Information:
- Supporting Information S1

Correspondence to:
L. Adam,
l.adam@auckland.ac.nz

Citation:
Adam, L., Frehner, M., Sauer, K., Toy, V., & Guerin-Marthe, S. (2020). Seismic anisotropy and its impact on imaging the shallow Alpine Fault: An experimental and modeling perspective. *Journal of Geophysical Research: Solid Earth*, *125*, e2019JB019029. https://doi.org/10.1029/2019JB019029

Received 7 NOV 2019
Accepted 7 JUN 2020
Accepted article online 24 JUN 2020

Abstract The transpressional Alpine Fault in New Zealand has created a thick shear zone with associated highly anisotropic rocks. Low seismic velocity zones and high seismic reflectivity are recorded in the Alpine Fault Zone, but no study has explored the underlying physical rock parameters of the shallow crust that control these observations. Protomylonites are the volumetrically dominant lithology of the fault zone. Here we combine experimental measurements of *P*-wave speeds with numerical models of elastic wave anisotropy of protomylonite samples to explore how the fault zone can be seismically imaged. Numerical models that account for the porosity-free real samples' fabric elastic tensors from electron backscatter diffraction (EBSD) are calculated by MTEX and a finite element model (FEM), while microfractures are modeled with differential effective medium (DEM) theory. At effective pressures representative of the Alpine Fault brittle zone, experimental wave speeds are lower than those predicted by MTEX/FEM. A possible DEM model suggests that a combination of random and aligned microfractures with aspect ratios increasing with pressure can explain the experimental wave speeds for pressures <70 MPa. Such microporosity in the form of foliation- and mica basal plane-parallel microfractures and grain boundaries is validated with synchrotron X-ray microtomography and transmission electron microscopy (TEM) images. Finally, by modeling anisotropy of seismic reflection coefficients with angle of incidence, we demonstrate that the high reflectivity and low-velocity zone (LVZ) observed at the Alpine Fault can only be explained if this microporosity is accounted for throughout the brittle fault zone, even at depths of 7–10 km.

1. Introduction

The internal structure of faults is studied by geophysical field observations (e.g., Chiu et al., 1992; Stern et al., 2007; Wannamaker et al., 2002), experimental studies (e.g., Gibson, 1998; Ikari et al., 2011; Niemeijer & Spiers, 2005; Reches & Lockner, 1994), and observations of paleofaults (e.g., Beck, 2009; Howarth et al., 2012; Wallace, 1981). Imaging fault zones develops our understanding of fault geometry at depth, which enhances our understanding of rupture mechanisms and thus hazard analysis, and also aids targeting in scientific drilling (Ma et al., 2006; Tobin & Kinoshita, 2006; Townend et al., 2009; Toy et al., 2015; Zoback et al., 2010). Both active and passive seismic surveys are used for this purpose (Feng & McEvilly, 1983; Hole et al., 1996; Zhao et al., 1993). But even for the best-designed seismic acquisitions, successful imaging of faults depends on their dip angle and the presence or absence of contrasting wave speeds and rock densities across the fault plane (Allmendinger et al., 1983; Kelly et al., 2017). A low-velocity fault damage zone is typically inferred from fault zone-guided waves (Li & Leary, 1990; Li et al., 1990). However, these inferences typically rely on a clear understanding of the fault zone geometry, elastic wave attenuation, and velocity contrasts (Ben-Zion, 1998). Although seismic wave anisotropy is central to crustal studies, it is commonly not taken quantitatively into account when processing seismic data in fault zones (Godfrey et al., 2002; Gulley et al., 2017; Leary et al., 1987; Simon et al., 2019). Nonetheless, wave anisotropy can be significant in fault zones due to intrinsic rock texture, such as crystallographic preferred orientation (CPO) and foliation (e.g., Burlini & Kunze, 2000; Johnson & Wenk, 1974; Jones & Nur, 1982; Kern et al., 2001; Shao et al., 2016; Wenning et al., 2016), and it can be exasperated by the presence of fractures and stress variations. No comprehensive study of elastic wave anisotropy that combines microstructural imaging, numerical

modeling, and experimental measurements has been performed to date in rocks representing the creeping shear zone beneath the Alpine Fault, New Zealand. In this study, we aim to answer what causes elastic wave anisotropy in these rocks in the shallow crust.

In the South Island of New Zealand, oblique continental collision between the Pacific and Australian plates is dominantly accommodated by the Alpine Fault. This fault has produced large earthquakes, M_w>7.6, rupturing on average every 330 years, with its last rupture in 1717 AD (Sutherland et al., 2007). Away from the narrow fault core composed of gouge and cataclasites (<∼30 m) is a 1-km-thick sequence of ultramylonites, mylonites, and protomylonites with foliations mostly parallel to the shear zone boundary (Norris & Cooper, 1997; Toy et al., 2008, 2017). However, at the base of the crust, the creeping shear zone could be up to 7 km thick due to shear shortening. These mylonitic rocks are derived from the micaceous quartzofeldspathic Alpine schist (Little et al., 2002), formed at depths greater than 15 km, but have been uplifted and are present throughout the brittle and ductile depths of the fault. Due to the fault motion, these mylonites have been rapidly uplifted to the brittle zone of the Alpine Fault and outcrop at several locations. Mylonites, protomylonites, and schist are volumetrically dominant in, and around, the fault zone. Cataclasites and ultramylonites only account for up to 100 to 150 m fault perpendicular thickness of the Alpine Fault lithology (Sutherland et al., 2015); therefore, their contribution to seismic signatures is minor.

Ductile deformation in shear zones results in micas having strong preferred orientations. This, combined with the high anisotropy of single mica crystals, results in high elastic wave anisotropy in mylonite rocks (Barruol et al., 1992; Cholach & Schmitt, 2006; Christensen, 1965, 1989; Dempsey et al., 2011; Fountain et al., 1984; Jones & Nur, 1984; Ji & Salisbury, 1993; Kern & Wenk, 1990; Khazanehdari et al., 1998; Shaocheng et al., 1993). Many shear zones have been identified to show high seismic reflectivity (e.g., Fountain et al., 1984; Ji et al., 2003; Jones & Nur, 1982; Rey et al., 1994; Stern et al., 2007; Wang et al., 2005; Wenning et al., 2016). To explain such reflectivity, mostly numerical approaches use normal incidence isotropic models (Christensen & Szymanski, 1988; Fountain et al., 1984; Jones & Nur, 1982; Khazanehdari et al., 1998; Rey et al., 1994; Shaocheng et al., 1993; Wang et al., 1989; Wenning et al., 2016). Few studies have performed anisotropic seismic processing and explored the effect of incident angle on seismic reflectivity in shear zones (Barruol et al., 1992; Khazanehdari et al., 1998; Simon et al., 2019).

At the Alpine Fault, seismic reflections and wave speeds of the upper surrounding lithosphere have been derived from active source seismic studies (Lay et al., 2016; Stern et al., 2007), and similar information has been determined with passive seismic methods up to 35 km in depth (Eberhart-Phillips & Bannister, 2002; Eccles et al., 2015; Feenstra et al., 2016). Seismic anisotropy in the vicinity of the Alpine Fault has been studied in the field (Karalliyadda & Savage, 2013), through numerical models (Dempsey et al., 2011; Godfrey et al., 2002; Gulley et al., 2017) and experiments (Allen et al., 2017; Christensen & Okaya, 2007; Okaya et al., 1995). At the Alpine Fault, seismic low-velocity zones (LVZs) (Feenstra et al., 2016; Lay et al., 2016; Stern et al., 2001; Stern et al., 2007) in the brittle upper crust and high reflectivities (Lay et al., 2016; Stern et al., 2007) are observed in seismic surveys. In some studies it is suggested that fluids are responsible for these LVZs and high fault reflectivity (Feenstra et al., 2016; Stern et al., 2001, 2007; Wannamaker et al., 2002), but only little physical evidence from elastic core-scale measurements or modeling exists (Simpson et al., 2020). Moreover, although the anisotropic nature of Alpine Fault rocks is known (Christensen & Okaya, 2007; Karalliyadda & Savage, 2013; Okaya et al., 1995), it is still mostly unknown how rock microstructure influences the observed anisotropy (Simpson et al., 2020) and its role on seismic reflectivity at the Alpine Fault. Therefore, there is a need to understand how mylonite rock physical properties relate to seismic signatures and microstructures. Our goal is to present a multimethod approach on a protomylonite rock sample to study the underlying physical properties that cause seismic anisotropy in the Alpine Fault with the goal of explaining the observed high fault reflectivity and LVZs in the brittle section of the fault.

Elastic wave anisotropy of hand specimens can be estimated by a range of methods, but most commonly by ultrasonic wave propagation (Birch, 1961) or numerical modeling based on electron backscatter diffraction (EBSD) data or neutron diffraction (e.g., Almqvist & Mainprice, 2017; Almqvist et al., 2013; Ji et al., 2003; Lokajíček et al., 2014, 2017; Mainprice & Nicolas, 1989; Zhong et al., 2014). EBSD data provide dense mapping of the CPO and compositional layering of constituent minerals. Wave velocities are numerical modeled from EBSD data by a Voigt-Reuss-Hill averaging of the zero-frequency (static) effective medium elastic

tensor (Dempsey et al., 2011; Ji et al., 2003; Mainprice & Nicolas, 1989) or with dynamic simulation of wave propagation using a finite element model (Zhong et al., 2014).

For shear zone rocks, there is strong literature on the controls of crystal-, lattice-, and shape-preferred orientations (CPO, LPO, and SPO, respectively) of the rock-forming minerals complemented with experimental ultrasonic data (e.g., Almqvist et al., 2013; Barruol et al., 1992; Burlini & Kunze, 2000; Ji et al., 2003; Kern & Wenk, 1990; Khazanehdari et al., 1998). Although these studies acknowledge the presence of microfractures, they focus on the effects of CPO, LPO, and SPO on the elastic anisotropy of shear zone rocks at pressures greater than 100–200 MPa. Because earthquakes in the Alpine Fault happen at shallow depths (<12 km), we set out attention to characterizing fractures and their influence on LVZ and reflectivity in the upper crust. Few studies have targeted quantifying microfractures in shear zone rocks by combined laboratory ultrasonic data and elasticity modeling based on EBSD and differential effective medium (DEM) (e.g., Almqvist et al., 2013; Kern & Wenk, 1990; Simpson et al., 2020; Sun et al., 2012). Based on EBSD, Zhong et al. (2014) compare experimental ultrasonic wave speeds to FEM for a phlogopite-bearing harzburgite with a fracture, while Morales et al. (2018) compare mantle conditions laboratory ultrasonics to MTEX and DEM modeling for an antigorite-olivine schist, though the analysis was not performed on the exact same sample. Almqvist et al. (2013) combine numerical modeling of EBSD, experimental wave speeds, and microfracture imaging to study and point at the possibility that microfractures could remain open at high effective pressures. Recently, Simpson et al. (2020) measure with a unique technique multidirectional wavespeeds to characterize seismic anisotropy and fractures on Alpine Fault rocks up to 1 km in depth. The objective of our study is to estimate elastic wave anisotropy on heterogeneous micaceous quartzofeldspathic mylonite samples from the Alpine Fault by studying the contributions of CPO, texture, and microfractures. This is achieved by comparing two types of numerical modeling (MTEX and FEM) combined with two laboratory studies (laser and transducer ultrasonics). The fractures are identified with microimaging analysis and a possible model based on a DEM theory. The laboratory and numerical results are used to study the implication of anisotropy and microfractures on the Alpine Fault seismic reflectivity and LVZs.

2. Samples and Methods

The micaceous quartzofeldspathic protomylonite sample that is the focus of this study comes from Stony Creek, in the central Alpine Fault shear zone (Figure 1). The exposed protomylonites from the Alpine Fault hanging wall are the dominant lithology of the shear zone and were deformed under similar conditions to those currently experienced in the active shear zone at depth (Dempsey et al., 2011; Toy et al., 2008). They accommodated most of the deformation that generated their tectonite fabrics at depths between 8 and 35 km and then were rapidly (<3 Ma) uplifted and exposed due to the fault's thrust slip component. We study one cylindrical sample with a diameter of 25 mm and 39 mm in length. On average, the sample's mineralogy is 42% quartz, 19% oligoclase feldspar, 35% phyllosilicates (dominantly biotite with muscovite and chlorite), and minor calcite, garnet, and accessory minerals such as tourmaline (Table 1). In the hanging wall of the fault zone at the sampling location, the Alpine schist commonly has a planar foliation defined by alternating layers of mica and quartz + feldspar. In protomylonite samples this foliation is overprinted by a mylonitic fabric, most obviously manifesting as millimeter to centimeter-spaced shear bands that form at depth by ductile creep mechanisms (Gillam et al., 2014; Toy et al., 2012, 2015). These mylonitic fabrics mature toward the PSZ, resulting in textural homogenization, grain size reduction, and mineral-phase mixing (Toy et al., 2008, 2012, 2015). Our samples are similar to those described by Toy et al. (2008, 2012, 2015) and only differ from protomylonites described in previous publications in the precise modal mineral composition (Table 1).

Figure 2 shows the protomylonite sample and the elastic wave experimental setups. Visually, the sample shows foliation heterogeneity, which was the reason for choosing this sample. To study heterogeneity, we cut two sections, from the top and bottom end of the sample, and prepare thin sections. Typical mylonitic fabrics are apparent in scans of these petrographic thin sections (Figure 2). These two sections are used for the EBSD analysis. Laser scans are also acquired at two locations (rotational sections) on the sample toward the top and bottom as shown in Figure 2. Differently, transducer ultrasonic data are acquired for vertical propagation (wave raypath is parallel to cylinder axis) on the whole sample with 25-mm-diameter *P*-wave transducers, and for horizontal propagation (wave raypath is perpendicular to cylinder axis and across the foliation), 8-mm-diameter transducers are used.

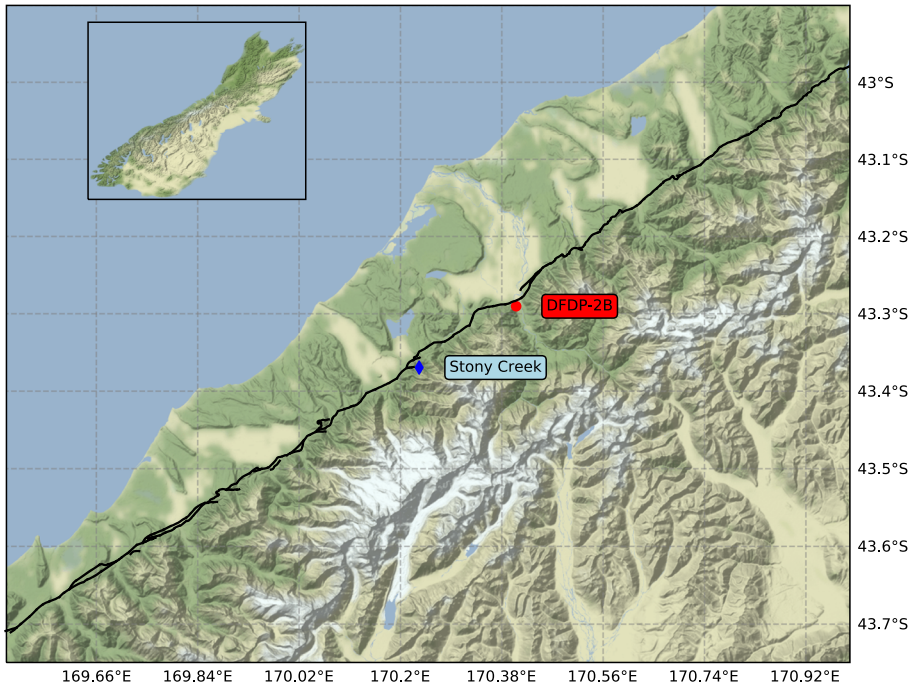

Figure 1. Map of the location of Stony Creek in the central Alpine Fault where the protomylonite rock sample is collected. The location of the ICDP Alpine Fault fault drilling project borehole (DFDP-2B) is marked for reference. Shown in black is the NE-SW-trending fault trace (data from the GNS Science Active Faults Database; Langridge et al., 2016).

EBSD data are acquired from the two polished petrographic thin sections using a Zeiss Sigma VP FE-SEM fitted with an Oxford Instruments HKL INCA Premium Synergy Integrated ED/BSD system, housed at Otago Microscopy and Nano-Imaging (OMNI). The SEM is operated with an accelerating voltage of 30 keV and a 300 mm aperture at a working distance of ~28 mm. EBSD patterns are acquired at a step size of 7 microns and processed with Aztec software to yield maps of mineral phases and crystallographic orientation from the the polished thin sections (Figures 2 and 3). Data are initially cleaned by wild spike removal and nearest-neighbor noise reduction in CHANNEL5 HKL Software (see Bestmann & Prior, 2003) to yield Channel Text Files (.ctf) that are the input for models of elastic wave propagation. The rock sections imaged by EBSD are cut perpendicular to foliation to preserve their textural information, particularly the distinct layering of quartzofeldspathic and micaceous domains. However, this made it particularly difficult to polish the fine-grained micas, making it even more difficult than usual for this phase to index them by EBSD. Dempsey et al. (2011) are also unable to recover EBSD mica information from Alpine Fault mylonites in sections cut perpendicular to foliation. They note that indexing is better for samples cut at low angles to foliation. Prior et al. (2009) also discuss that reliable acquisition of EBSD data from fine-grained micas is challenging, due to the platy habit of the mineral. Based on microphotograph observations from Toy et al. (2008) and Dempsey et al. (2011), we determine that most of the nonindexed phases (black in Figure 3) are muscovite or biotite with their basal planes aligned parallel to foliation, and for subsequent modeling of static and dynamic elastic wave anisotropy, we assign all nonindexed phases as muscovite since this mineral has very similar elastic properties to biotite.

Table 1
Volumetric Mineral Contributions (in %) From SEM Phase Identification Corresponding to the FEM and MTEX Simulated Areas in Figure 3

Mineral	Qz	Olig	Bio	Mus + non-ind	Clino	Cal	Pyr
PM-1 FEM	51.21	16.13	1.23	30.66	0.03	0.74	0.01
PM-1 MTEX	51.03	16.71	1.20	30.34	0.03	0.69	0.01
PM-2 FEM	31.61	27.63	0.17	34.81	0.03	1.75	0.01
PM-2 MTEX	35.19	19.98	2.07	39.18	1.72	1.61	0.26

Note. Qz = quartz; Olig = oligoclase; Bio = biotite; Mus + non-ind = muscovite + nonindexed; Clino = clinochlore; Cal = calcite; Pyr = pyrope.

We estimate and compare elastic wave anisotropy of the sample by combining the following experimental and numerical methods:

- Experimental transducer ultrasonic measurements: *P*-wave anisotropy at effective stresses up to 64 MPa.

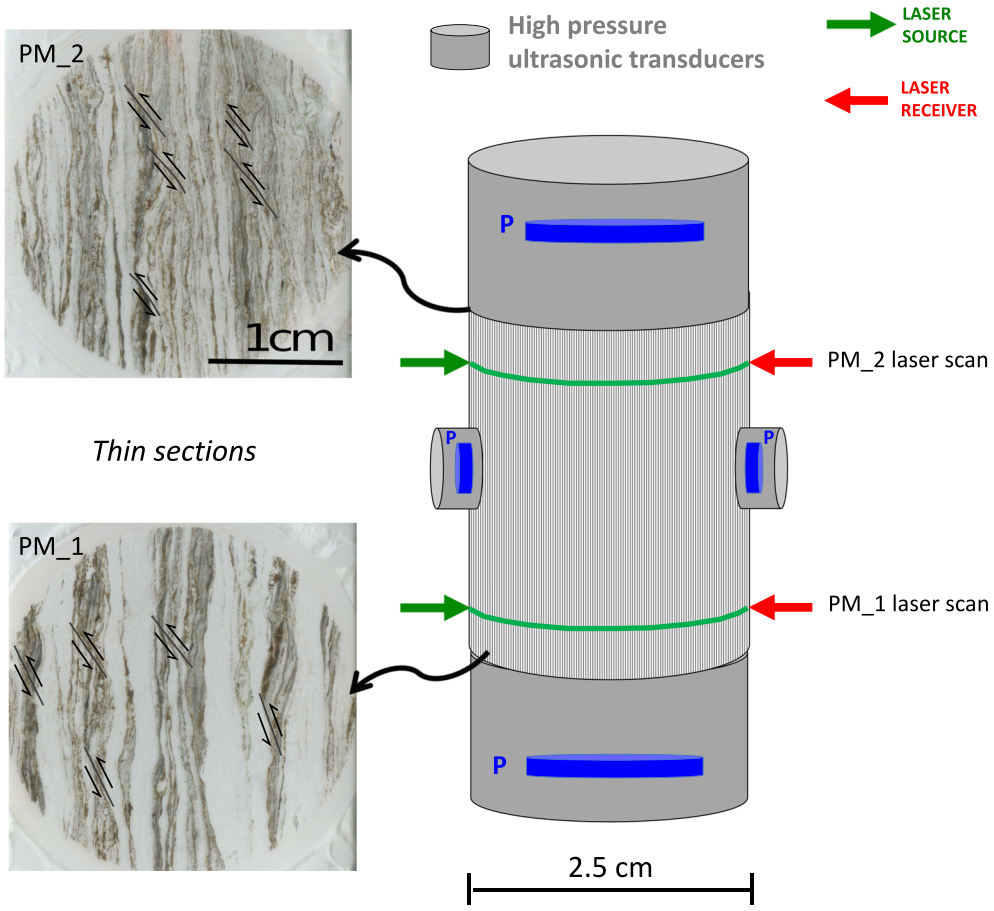

Figure 2. (left) Scans of petrographic thin sections of the top and bottom of the sample with labeled shear bands. (right) Laboratory setup for laser and high pressure transducer ultrasonics. Laser data are acquired at two locations close to the sample edges. Transducer data are acquired parallel to foliation with 25-mm-diameter transducers and perpendicular to foliation with 8 mm transducers.

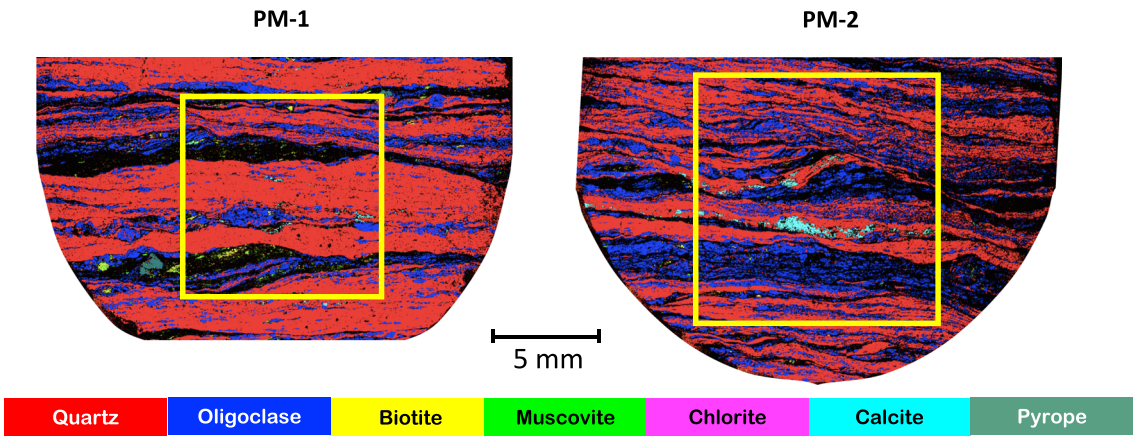

Figure 3. EBSD mineral phases on the two mylonite samples from Figure 2. Black represents nonindexed phases. The yellow box is the area simulated by both FEM and MTEX.

- Experimental laser-ultrasonic high-density sampling: anisotropy symmetry validation and *P*-wave anisotropy at atmospheric pressures.
- MTEX modeling: predict zero-frequency (static) *P*-wave anisotropy and symmetry for a porosity-free mylonite. Compositional layering is not accounted for in the modeling.
- Finite element model (FEM): predict dynamic *P*-wave anisotropy and symmetry for a porosity-free mylonite. Compositional layering is accounted for in the modeling.
- DEM modeling: predict volume, shape, and orientation of open microfractures with effective pressure.

Figure 2 is a sketch of the laser and transducer ultrasonic sample setups. The laser-ultrasonic system (LUS) has a source and receiver footprint diameter of 4 and 2 mm, respectively. For highly anisotropic rocks, the effect of beam skew for propagations away from normal and parallel to foliation has been recently highlighted by Li et al. (2020). However, due to the small footprint of the lasers, this effect does not influence the laser-ultrasonic data. In comparison, transducers commonly have a footprint of 25 mm. At atmospheric conditions, we acquired waveforms with the LUS, where a high-energy pulsed laser excites ultrasonic waves via thermoelastic expansion on the sample surface. The initial mode generates *P* and surface waves, but *S* waves are also present due to reflection and transmission conversion. The source and receiver lasers are aligned on opposite sides of the sample (Figure 2), and waves are detected using a laser vibrometer, which measures the displacement at the sample surface due to a wave perturbation (for details, see Blum et al., 2013; Simpson et al., 2019). The sample is rotated at 1° increments on a computerized stage, and data acquisition is automatized (Johnson et al., 2014). Figure 2 shows that there are two *rings* close to the sample edges (red and green arrows) where waveforms are acquired as a function of angle to foliation (waveform data are presented in supporting information Figure S1). From the waveforms, we pick the arrival times for the direct *P* wave and estimate wave speeds as a function of propagation angle.

A transducer ultrasonic system is used to record *P* waveforms for propagation in two directions: parallel and perpendicular to foliation from ambient to confining pressures of 64 MPa (waveforms shown in Figure S2). Hydrostatic confining pressure is applied with hydraulic oil. The dominant frequency of our recorded ultrasonic signals is on average 600 kHz. We pick between 10 and 20 arrival times and estimate the picking time random error from this distribution. These errors together with the random error in sample length are propagated into the wave speed errors. We saturated the sample with distilled water at a fluid pressure of 1 MPa, but connectivity between the top and bottom fluid lines is not achieved despite waiting for 2 weeks due to very low permeability. From here on, we refer to effective pressure, which is the difference between confining and fluid pressures, assuming an effective stress coefficient of 1.

The MTEX and FEM models are both performed on the yellow areas highlighted in Figure 3. Table 1 is the volumetric contribution of the different mineral phases within each of these areas. Slight differences result from how the FEM rotates the EBSD model (see section S3). The stiffness tensor used for each mineral in both modeling methodologies is in Table S4.

MTEX modeling uses the open-source MTEX toolbox for MATLAB (Bachmann et al., 2010; http://mtex-toolbox.github.io/), where pixels indexed by EBSD are converted to grains using Voronoi decomposition (Bachmann et al., 2011), with grain boundaries defined using a misorientation angle of $\geq$10° (Shigematsu et al., 2006). Modeling of seismic properties uses scripts available in the MTEX toolbox and follows the method explained by Mainprice et al. (2015). It is essentially a summation of the elastic tensors for each constituent mineral with the orientation determined at that indexed point in the EBSD data set.

The principle of the FEM is described in Zhong et al. (2014), which is based on developed code by Frehner et al. (2008), Frehner (2013), and Frehner and Schmalholz (2010). The method uses a 2-D plane strain formulation of the governing force balance and the linear elastic rheological equations. In comparison to the MTEX method, the FE model is discretized with the same detail as the EBSD pixel sampling. This gives the code power to include the influence of the rock texture (compositional layering) on wave propagation. The code could also handle porosity (Zhong et al., 2014), but we do not use this option in this study as our objective is to compare MTEX, FEM, and laboratory data acquired from the same sample. Moreover, we were unable to distinguish porosity with EBSD and thus could not model its contribution with FEM. A compressional plane wave is propagated from the left to the right side of the EBSD model (see section S3). Wave propagation simulation is performed for different angles, with a 10° step from 0° to 180°. We use a source Ricker wavelet with a 600 kHz dominant frequency to match the laboratory data;

343 individual traces are recorded on the right edge of the model, which are later stacked to produce one trace (section S3). For the FEM, five different models with variable isotropic and anisotropic mineral contributions are compared:

1. *Indexed minerals isotropic and muscovite isotropic:* The stiffness tensor of each of the minerals (Table S4) is averaged using Voight-Reuss-Hill to resemble an isotropic mineral.
2. *Indexed minerals anisotropic and muscovite isotropic:* The stiffness tensor of all minerals but muscovite is anisotropic (Table S4). The stiffness tensor of the muscovite minerals is averaged using Voigt-Reuss-Hill to resemble an isotropic mineral.
3. *Indexed minerals anisotropic and muscovite average anisotropic:* The stiffness tensors of all minerals are anisotropic (Table S4). Nonindexed phases are assigned to the averaged indexed muscovite anisotropic tensor.
4. *Indexed minerals anisotropic and muscovite anisotropic parallel to foliation:* Indexed mica volumes are small (<1%), as most of the micas cannot be indexed. For 1, 2, and 3, the few indexed muscovites are modeled as either isotropic or anisotropic crystals. However, these few micas have randomly distributed Euler angles for their basal planes, and we know these do not represent the true distribution of muscovite in these rocks. We therefore assign all nonindexed phases to muscovite with their basal plane parallel to foliation.
5. *Static:* The area of the EBSD is deformed statically (zero frequency) in a uniaxial compression. The boundary conditions are compression on one side of the model, and no deformation is allowed in any of the other three directions. This simulation gives a steady-state stress-strain relationship at every numerical point of the model. All the stress and strain components are averaged to produce the static elastic moduli in that direction of compression.

Compressional or *P*-wave wave anisotropy ($V_{P,\text{aniso}}$) is estimated as the ratio between the fastest ($V_{P,\text{fast}}$) and slowest ($V_{P,\text{slow}}$) wave speeds. $\bar{V}_P$ is the mean value of these two speeds. In a transversely isotropic media (i.e., layered), such as foliated metamorphic rocks, the fast propagating waves are associated with propagation parallel to foliation, while the slow propagating waves travel perpendicular to foliation:

$$V_{P,\text{aniso}} = \frac{V_{P,\text{fast}} - V_{P,\text{slow}}}{\bar{V}_P} \tag{1}$$

We model the fast and slow elastic wave velocities by following the DEM approach of O'Connell and Budiansky (1974) and Bruner (1976) (Figure 7). We use a modified version of the DEM GassDem code by Kim et al. (2019) that mixes parallel to foliation and randomly distributed microfractures (Simpson et al., 2020). The DEM builds on the MTEX porosity-free stiffness tensor derived from EBSD. Fracture porosity, aspect ratio, and random versus aligned fractures modeled at each effective pressure are summarized in Table S6. Porosity for the DEM modeling is obtained from a similar mylonite rock at atmospheric conditions (Simpson et al., 2020) and qualitative fracture distributions from X-ray microtomography. It is important therefore to understand that the model proposed here is one of many possible fracture models that describe our data.

Finally, we have undertaken microstructural characterization of fractures and pore space within the samples, employing a combination of transmission electron microscopy (TEM) and synchrotron X-ray microtomography (sCT) at atmospheric conditions. Thin lamellae for TEM observation are extracted from the samples via focused ion beam (FIB) milling, and high-resolution images are acquired from these lamallae on an FEI Tecnai G2 F20 X-Twin transmission electron microscope, located at the German Research Centre for Geosciences (GFZ), Potsdam, Germany (Figure 6). The instrument is equipped with FEG electron source and HAADF Detector. Images are collected from samples placed on a Gatan double-tilt holder at 200 kV (Kruhl et al., 2013; Wirth, 2004).

We acquired the X-ray microtomography data for this study on beamline 20XU at SPring-8, Japan. The samples are cylinders 3 mm in height and 1 mm in diameter. They are mounted on a rotary stage and imaged with a beam energy of 20 keV. We acquire scans using a visible-light conversion-type X-ray detector with CMOS camera at 0.1° rotation steps over 180°. Reconstruction is undertaken using a convolution back projection method. Micro-sCT scans of the entire samples are reconstructed at a minimum effective voxel size of

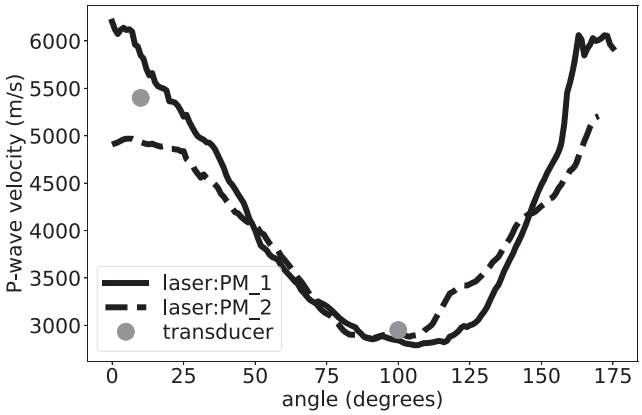

Figure 4. Wave speeds at the top and bottom locations of the sample (see Figure 2) acquired with the laser-ultrasonic system. Transducer ultrasonic data are acquired parallel and perpendicular to foliation. All data are acquired at atmospheric conditions.

0.524 μm. Data analyses and image processing are performed using the commercial software package Avizo 9.1. Initially, the data sets are rescaled to 8-bit volumes for enhanced computer performance. In addition, small volumes of interest are cropped from the whole volume before a nonlocal mean filter is appliedto reduce noise. The gray-scale values corresponding to porosity are thresholded, yielding the 3-D images illustrated in Figure S5. These red-cyan stereo images are generated using Avizo 9.1 built-in functions.

3. Results

3.1. Experimental *P*-Wave Speeds at Atmospheric Pressures

We first present *P*-wave speed as a function of propagation angle based on laser and transducer ultrasonic measurements at atmospheric conditions. Figure 4 presents the speeds with propagation angle at two locations on the sample (Figure 2). First, we observe that the sample has an elastic symmetry close to vertically transversely isotropic. Fast waves propagate parallel to foliation, while slow waves propagate perpendicular to foliation. Wave speeds for propagation normal to foliation are similar for both laser scans. However, wave speeds for propagation parallel to foliation vary significantly between the two scans. On closer inspection, the distribution of mineral phases in the fast wave speed direction (foliation parallel in the center part of the sample) between the top and bottom of the sample varies: PM-1 has thick bands of micas, while PM-2 has a mixture of quartzofeldspathic bands. Because the laser source and receiver have small footprints, 4 and 2 mm, respectively, we are able to record wave arrivals of *guided* waves within these variable-width mineral bands. Muscovite and biotite minerals in this rock are mostly aligned with their basal planes parallel to foliation. These micas are intrinsically anisotropic with the highest elastic moduli (and thus wave speed) in the direction parallel to the basal plane (c_{11} and c_{22} from Table S4). The phenomenological interpretation is that in such anisotropic rocks, the wavefront deforms from perfectly spherical, where some sections of the wavefront travel faster if propagating parallel to foliation in the mica band. Other parts of the waveform lag behind these fast mica bands if propagating through quartz and plagioclase bands, where wave speeds are lower than those parallel to the basal plane of the micas. For propagation normal to foliation, such *guided* waves do not develop in a perpendicular raypath as the wavefront crosses all bands, and thus, band thickness and mineralogy do not significantly influence the wave speed measurements in the slow propagation direction. The latter only holds when the total volumetric contribution of phases is similar between these two sections, such as in our samples (Table 1).

We compare the laser wave speed data to transducer ultrasonic data (Figure 4). Olympus ultrasonic transducers for atmospheric pressures have a footprint diameter of 38 mm, having a significantly greater area to emit and receive the ultrasonic waveforms compared to the laser system. A large received footprint averages the different parts of the wavefront arrivals and will be less sensitive to the *guided* waves. Furthermore, the transducer wave is propagated through the whole sample, along the axis of the cylinder (Figure 2), thus averaging textural variations in the sample. As expected, the measured slow wave speed (perpendicular to foliation) matches that of the LUS. However, the wave speed in the direction parallel to foliation averages the deformed wavefront propagating through mica- and quartz/feldspar-dominated layers. These observations are important when interpreting experimental and modeling data where sample heterogeneity due to mineral banding can influence wave propagation and the recorded experimental wave speeds. We will support this experimental observation with final element modeling that takes into account compositional layering data from EBSD mapping.

3.2. MTEX and FEM Modeling of EBSD Data

The MTEX-modeled *P*-wave speeds for the two thin sections, illustrated on lower-hemisphere and equal-area projections, show that the effective anisotropy symmetry of these porosity-free samples is similar (Figure 5). The orientation of this plot matches the orientation of the EBSD map (Figure 3). *P*-wave anisotropy is estimated using Equation 1 from the minimum and maximum wave speeds in these plots. The *P*-

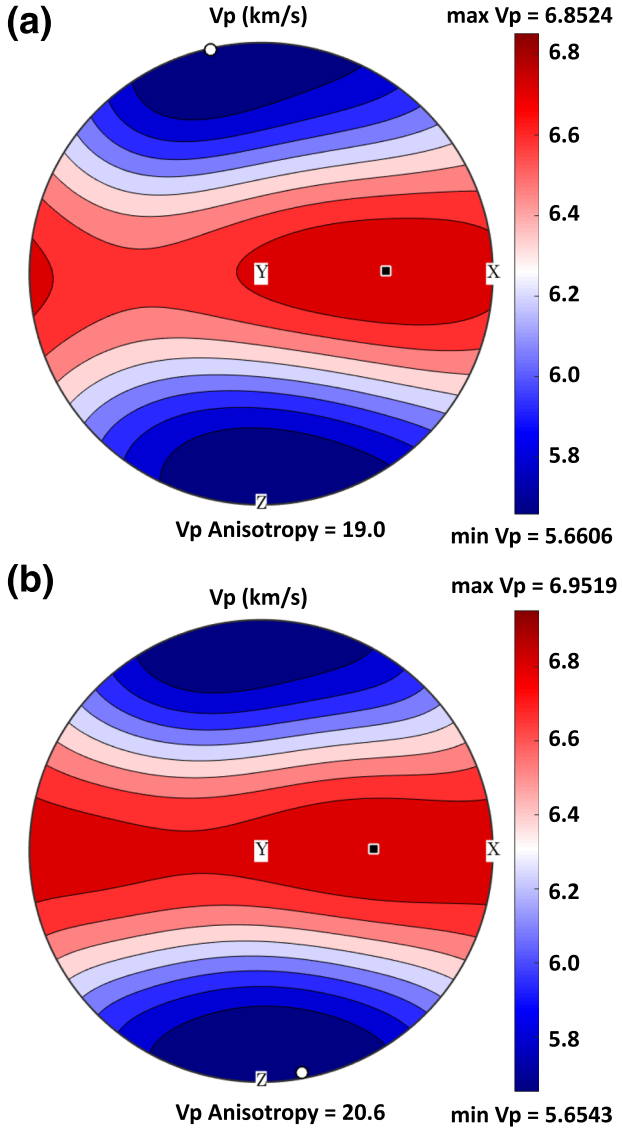

Figure 5. MTEX-modeled *P*-wave speeds (V_P) based on EBSD images in Figure 3 on lower-hemisphere, equal-area stereographic projections. (a) PM-1 and (b) PM-2. Here, unindexed phases are assumed to be muscovite with their basal plane aligned parallel to the foliation plane, while all other minerals are modeled with phases and crystallographic orientations based on EBSD analysis. All phases are modeled as anisotropic minerals. Black square and white circle locations represent the maximum and minimum V_P, respectively, also reported in the color bar.

wave velocity anisotropy of these two samples is similar, at 19.0% and 20.6% for PM-1 and PM-2, respectively, probably because these samples have similar modal mineralogy (Table 1).

The *P*-wave propagation wave speeds with FEM for the two thin sections are illustrated in Figure 6. The different modeling approaches (lines) are described in section 2. One of our models assumes that micas are elastically isotropic crystals so that we can study the effect quartz and feldspar alone have on elastic anisotropy (red curve in Figure 6). Due to the wide varieties of orientations of *c* axes for quartz and feldspar and their low intrinsic elastic anisotropy (compared to micas), the total modeled anisotropy due to these two minerals is low: 2.36% and 0.74% for PM-1 and PM-2, respectively. The modeled velocities illustrated by the green line only account for the indexed micas, which as previously discussed, are not representative of the dominant CPO of the micas in these rocks. The main result from FEM that we compare to MTEX and experimental data is the black curve. We reiterate that in both FEM and MTEX calculations, all nonindexed phases are assumed to be muscovite with their basal planes parallel to the rock foliation. The anisotropy estimated by FEM is significant, with similar anisotropy estimates as for the MTEX modeling: 20.2% and 21.9% for PM-1 and PM-2, respectively. The MTEX-modeled speeds are consistently higher than for the FEM, as is illustrated by the gray (MTEX) and black (FEM) lines on Figure 6. However, reassuringly, the wave speed angle dependence (line shapes) that is very similar among both and MTEX is still within the upper limit of the FEM simulations (gray-shaded area, see section S3 for the explanation of these). The MTEX method is a static (zero-frequency) method that employs effective medium averaging of the stiffness tensor of the EBSD-mapped phases and their crystallographic orientations. In contrast, FEM is a dynamic method, and the propagation of the wave through mineral phases with a variety of orientations as indicated by the EBSD analyses can result in wave scattering. Wave scattering, which occurs when there are high seismic impedances between grains or layers in a rock, can result in slower wave speeds. To confirm if scattering has a significant effect on wave speeds, static deformation using a FEM approach is tested. The static-derived wave speeds calculated by FEM (dotted lines in Figure 6) are still lower than those derived from the MTEX method. As the input parameters to both methods are identical, we can only conclude that the way the methods approach averaging of the stiffness tensor over the whole EBSD section results in wave speed variations between the two methods by ±100 m/s.

The lines in Figure 6 are the averages of 343 dynamic wave propagation recordings for a particular angle (section S3). However, all the 343 waveforms are included in the gray-shaded areas of these plots. The dynamic nature of the FEM tool takes into account the distribution of phases and thus rock texture. Section S3 shows how the plane wavefront deforms due to the rock texture and phase-type distribution. The receivers are aligned along one side of the model and thus record the distorted nature of the wavefront. As such, the FEM supports our observation of *guided* waves recorded with the LUS. It is clear from these plots that wave speeds, and thus the estimates of elastic wave anisotropy, are sensitive to the modeled wave pathway within the EBSD map and the modeling tool. From the gray-shaded areas, wave speeds in the fast direction can vary between 6,381 and 6,965, and 5,276 to 5,590 m/s in the slow direction. This results in estimates of *P*-wave anisotropies that vary between 13% and 27% if specific source-receive paths are analyzed.

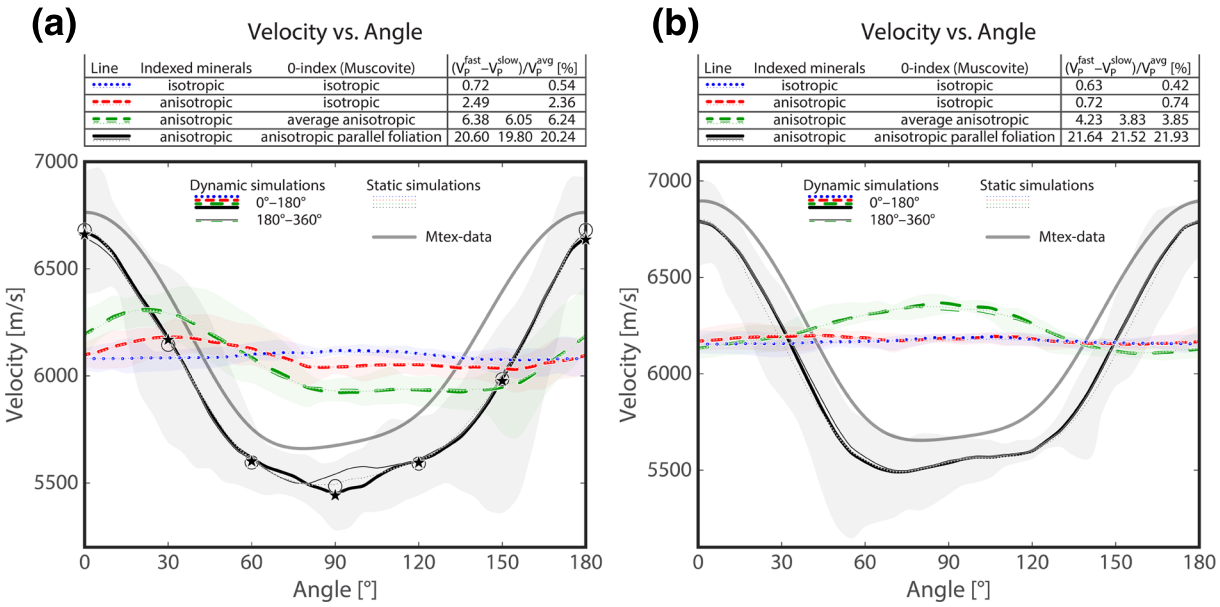

Figure 6. Finite element method-modeled *P*-wave speeds based on EBSD images in Figure 3. (a) PM-1 and (b) PM-2. The effects of mineral isotropy and anisotropy are compared. Gray-shaded areas are all possible models from FEM (section S3), while solid lines are the averaged values for that particular model. All unindexed phases are assumed to be micas with their basal planes parallel to the foliation plane, while all other phases have CPOs based on EBSD results. Gray solid lines are V_P values extracted from the primitive of the lower-hemisphere, equal-area projections showing the results of MTEX modeling results (Figure 5). This corresponds to the in-plane velocity within the thin section and matching the same propagation angles as for the FEM. Anisotropy values in the top tables refer to maxima, minima, and averages of all 343 FEM recordings (left, center, and right columns).

3.3. Experimental *P*-wave Speeds at High Effective Pressures

Experimental ultrasonic data under effective pressure are analyzed and compared to the MTEX and FEM results. Figure 7 plots wave speeds measured parallel and perpendicular to foliation as a function of effective pressure. The most significant nonlinear increase in wave speeds occurs between 0 and 40 MPa. For effective pressures greater than 40 MPa, the velocity data show a linear trend. DEM modeling of fracture porosity, aspect ratio, and random versus aligned fractures as a function of each effective pressure is shown in Figure 7, and model parameters are listed in Table S6. It is important to remember that DEM modeling is nonunique, and thus, the model proposed here is one of many possible fracture models that describe our data, but which is supported by experimental and microimaging analysis.

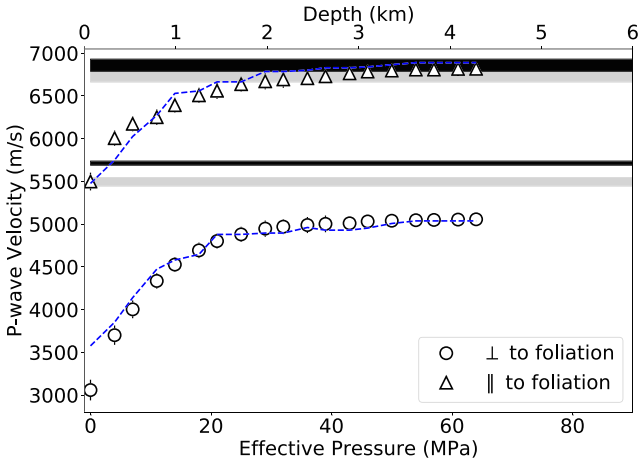

Figure 7. Ultrasonic *P*-wave velocity measurements under effective pressure. Transducers are placed at the top (parallel to foliation) and side (perpendicular to foliation) of the sample as shown in Figure 2. Markers are the ultrasonic experimental data. One standard deviation error bars are the size of the markers or smaller. Mineral-phase-only MTEX and FEM models include the wave speed data for both PM-1 and PM-2 (gray and black bars, respectively). Effective pressure is converted to depth assuming hydrostatic fluid pressures and density of protomylonites of 2,670 kg/m^3. The dashed blue line is the DEM modeling of anisotropic wave speeds by combining porosity-free rock elastic anisotropy and microfractures.

3.4. Evidence of Microfractures

Open grain boundaries, which form due to elastic contraction of the quartz grains during exhumation, and microfractures are revealed in HAADF images of our protomylonite sample and on three-dimensional images derived by sCT from a similar protomylonite sample from Stony Creek (Figure 8). It is only at these scales of observation that open grain boundaries (Kruhl et al., 2013) are clearly visible in these Alpine Fault rocks. Some of these grain boundaries are filled with amorphous silica (Figure 8a). Fracture network renderings from sCT additionally highlight substantial porosity aligned with mica basal planes and foliation, along with the aforementioned grain boundaries around quartz and feldspars, which have aligned and random orientation distribution (Figure 8b).

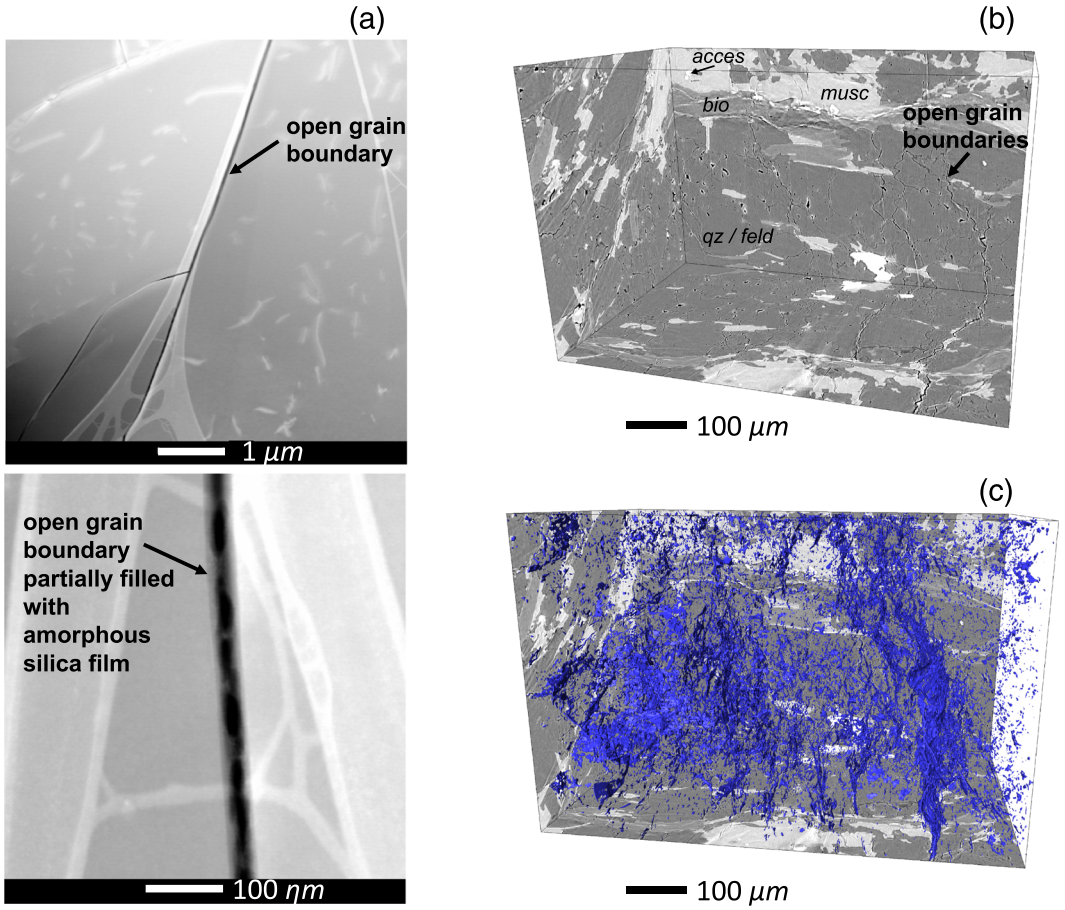

Figure 8. TEM-HAADF images of the protomylonite in this study (a) and synchrotron X-ray microtomography (sCT) on another Alpine Fault protomylonite from Stony Creek (OU86066) (b,c). (a) Top: open grain boundary (darker than the surrounding material) and a microcrack. (a) Bottom: zoomed section of the previous boundary demonstrating it is partially filled by an amorphous silica film. (b) sCT image showing microfractures, open grain boundaries, and minerals, all of which have different gray shades related to their density and X-ray absorbance. The view is in line with the foliation planes. (c) Fracture network rendering demonstrating microfractures and open grain boundaries from (b). A 3-D view of the fracture network is shown in Figure S5.

The Alpine Fault protomylonite was specifically selected for its heterogeneity. One objective is to study the influence of heterogeneity on experimentally measured and modeled wave speeds at the top and bottom locations of the sample and as a whole. For this heterogeneous protomylonite we observe that (1) fast *P*-wave speeds are influenced by the heterogeneity if the elastic sensor's source-receiver footprint is small, but this difference is averaged when a transducer samples the whole rock (Figure 4); (2) slow *P*-wave speeds are averaged as the elastic wave propagates through all the layers (Figure 4); and (3) *P*-wave velocity numerical models based on EBSD show similar sensitivity to layering heterogeneity and a significant effect on the predicted anisotropy with variations between 13% and 27% (Figure 6). When looking at evidence for microfractures, scale also plays a role. Microstructural imaging methods are bound to specific resolutions and sample size, meaning that the sampling of rock microstructures (e.g., microfractures and nanofractures) may differ between them. By contrast, ultrasonic waves record the average effect of all microstructures present in a rock sample, but suffer from individually distinguishing the effect of minerals, fractures, or fluids on wave speeds, and field representation. While effective medium theories can be used to estimate volume and shapes of fractures, these methods suffer from nonuniqueness. Nonetheless, although we measure only one rock sample in this study, we reconcile to the best of our knowledge the limitations of each of the methods and the effect of sample heterogeneity to provide possible interpretations to field seismic observations.

4. The Effect of Open Grain Boundaries and Microfractures on *P*-Wave Speeds

Ductile deformation in shear zones results in micas having strong preferred orientations. This, combined with the high anisotropy of single mica crystals, results in high elastic wave anisotropy in mylonite rocks (Christensen, 1965; Cholach & Schmitt, 2006; Dempsey et al., 2011; Fountain et al., 1984; Ji et al., 2003; Jones & Nur, 1984). We use mineral phase, CPO, and microstructural arrangement data to predict, using two independent methods, the porosity-free anisotropic wave speeds of a protomylonite rock. Strong VTI symmetry anisotropy in the order of 20% is observed from numerical models. However, small deviations from this symmetry are observed in laboratory measurements (Figure 4) and numerical modeling (Figure 5). These could be due to the shear bands in these samples, which perturb the strictly planar foliations (Lloyd et al., 2009).

Differences between modeled porosity-free wave speeds and laboratory data are commonly interpreted in terms of open fractures (Eberhart-Phillips et al., 1989; Schubnel & Guéguen, 2003; Shapiro, 2003). In the presence of background (i.e., porosity-free) anisotropy with randomly oriented fractures, the change in wave speed with pressure in the fast and slow direction is similar (Birch, 1961; Schubnel & Guéguen, 2003; Walsh, 1965). When fractures are aligned, however, *P* waves travel faster parallel to the fractures than perpendicular to them (e.g., Babuska & Cara, 1991; Crampin, 1984; Nur & Simmons, 1969b; Sayers & Kachanov, 1995) and the fast wave speed is less sensitive to fracture closure as pressures increase compared to the slow wave speed (Meléndez-Martínez & Schmitt, 2016; Schubnel & Guéguen, 2003; Simpson et al., 2020; Sun et al., 2012). But up to what effective pressures can we expect grain boundaries and microfractures to remain open in the Alpine Fault Zone?

We observe that laboratory fast and slow wave speeds are consistently lower than the numerically modeled porosity-free values (Figure 7). From this and DEM modeling we infer that the increasing wave speeds with effective pressure is due to the closure of grain boundaries and microfractures (natural and coring induced). At low pressures, wave speeds increase with pressure due to changes in the volume and shape of the microfractures, but when low porosity is reached, changes in wave speed are mostly due to fracture shape (Christensen, 1965). With increasing pressure, porosity does not necessarily need to all close (Garboczi et al., 1995; Gueguen & Dienes, 1989; Sarout, 2012; Sarout et al., 2017) and the aspect ratio of fractures increases (i.e., pores become rounder) (Sarout et al., 2017; Schubnel et al., 2006; Tsuji & Iturrino, 2008). Percolation theory describes that there is a point where, although the connectivity of the microfractures or grain boundaries is zero (permeability trends to zero), porosity does not necessarily have to be zero (Gueguen & Dienes, 1989; Sarout, 2012; Sarout et al., 2017). The amount of the remaining porosity depends on the assumed pore shape and number of fractures. Our DEM model assumes that at 60 MPa effective pressure, we still have a porosity of 0.5%. Such low porosity and below can still have a significant impact on wave speeds (Garboczi et al., 1995; Sarout, 2012). Our DEM protomylonite model suggests that as effective pressure increases from 1 to 60 MPa, porosity decreases from 4% to 0.5%, aspect ratio increases from 25-25-1 to 5-5-1, and percentage of aligned versus random fractures increases from 40:60 to 90:10 (Figure 7 and Table S6).

Although the imaging of the microfractures was done at atmospheric conditions, we can infer this evolution of such microfractures with pressure. The presence of amorphous silica within the grain boundary may mean that the grain boundaries do not completely close as effective pressures increase. Batzle et al. (1980) show that cracks like these, with rough, pitted, and mismatched walls, can remain open at high effective pressures. Furthermore, such irregular microfractures could lead to new fracture development where stress concentrates at asperities. Recently, Sarout et al. (2017) measured and modeled rock permeability and wave speeds as a function of pressure on a thermally cracked marble rock. They propose a similar crack evolution model as the one presented here to jointly explain their permeability and elastic wave data and models. At low effective pressures, opposing crack asperities are open, resulting in low aspect ratio microfractures. As effective pressure increases, these asperities contract, reducing the crack size and volume and increasing aspect ratio. Figure 9 is our proposed model of the closure of a grain boundary with increasing effective pressure, showing the evolution of aspect ratio from low to high. In an elastic regime as effective pressure increases (arrows), the uneven walls of the partially filled grain boundary join but do not fully close. Fractures aligned to foliation as well as those parallel to mica basal planes will create a greater pressure dependence for *P*-waves propagating normal to foliation ($V_{P,\mathrm{slow}}$) than those propagating parallel to the foliation plane ($V_{P,\mathrm{fast}}$). Although our model in Figure 9 is in two dimensions, we can extend our

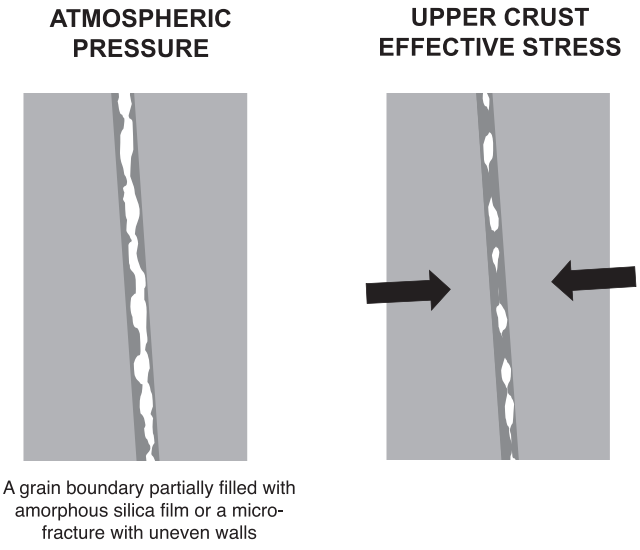

Figure 9. Model of an open grain boundary partially filled with amorphous silica film—dark gray—as shown in Figure 8a at atmospheric and high effective pressures. The model can also represent a microfracture with uneven walls. Arrows represent increasing effective pressure.

observation to 3-D microstructures by looking at the sCT image (Figure 8c) where several open grain boundaries extend/join into larger planar subparallel features. Under such a phenomenological model and MTEX and DEM modeling, we propose that fractures remain open high effective stresses in the brittle Alpine Fault.

On a set of different Alpine Fault rocks, Simpson et al. (2020) show that constraining fracture shape and volume can be improved by using more than two velocity data points per effective pressure. On a different protomylonite sample, they propose that at effective pressures below 16 MPa, 25% of the fractures are aligned. Still, the nature of effective medium modeling is that it builds on a range of free parameters, which we most of the time do not have a way to constrain. Moreover, we only modeled two distributions of fractures (random and aligned) with a unique aspect ratio per pressure point. However, it is possible that microfractures in rocks have at least a bimodal distribution of aspect ratios (Moyano et al., 2012) and fracture orientation is more complex than two sets of aligned and random microfractures. Including *S*-wave velocity information for the inversion of fracture volume and shape would be valuable (Sun et al., 2012).

Full closure of cracks is commonly assumed to happen at pressures greater than 200 MPa (Babuska & Cara, 1991; Brace, 1965; Birch, 1961; Ji et al., 2007). The indicator of such closure is the transition from a nonlinear to a linear relation between wave speeds and effective pressure. However, studies on mylonites and many other rock types have shown that the transition from nonlinear to linear velocity-pressure behavior in mylonites can be as low as 20 MPa (Burlini & Kunze, 2000; Ivankina et al., 2005; Jones & Nur, 1984; Kern & Wenk, 1990). Ji et al. (2007) and Wang et al. (2005) propose a linear velocity-pressure models for nonporous rocks. These models describe that the transition from nonlinear poroelasticity to linearity is due to the full closure of a single set of random fractures with constant shape (aspect ratio) as described by Walsh (1965). In such models, the linear wave speed increase is interpreted to be due to elastic mineral compressibility (Christensen, 1965). However, assuming fractures have a single aspect ratio and orientation at all effective pressures is simplistic in real rocks (Gueguen & Dienes, 1989; Sarout et al., 2017; Schubnel et al., 2006; Tsuji & Iturrino, 2008). Transitions from nonlinear poroelasticity to linearity can also be explained by combining compliant and stiff porosity (Eberhart-Phillips et al., 1989; Shapiro, 2003). After a rapid increase in wave speeds with effective pressure, the changes with increasing pressure are nearly linear while porosity is still nonzero (Eberhart-Phillips et al., 1989; Gueguen & Dienes, 1989), and with adequate fracture parameter, these linear trends can be modeled with DEM.

Lineation normal fractures, formed during exhumation, have been imaged in granulite mylonites (Ji et al., 1997, 2003). Almqvist et al. (2013) and Ivankina et al. (2005) invoke that microfractures, also linked to the structural lineation of the samples, can be responsible for differences between modeled and laboratory data. No lineation however is visible on our samples. This is expected since Alpine Fault mylonites are typically poorly lineated, or if lineations are present, their orientations do not reflect the strain kinematics of their most recent deformation regime (Toy et al., 2013). Most analyses on shear zone rocks point at the existence of microfractures from the sharp increase in wave speeds with pressure (e.g., Almqvist et al., 2013; Babuska & Cara, 1991; Burlini & Kunze, 2000; Kern et al., 2008); however, microfractures have not been at the center of the interpretation. Almqvist et al. (2013) image such microfractures with SEM and micro-CT on mylonitized carbonates and interpret their contributions at pressures below 200 MPa, suggesting that such fractures might not all be fully closed at pressures as high as 450 MPa. Kern et al. (2008) suggest that low aspect ratio intercrystalline and intracrystalline microfractures related to biotite minerals should close at high effective pressures (>100 MPa), but Kern and Wenk (1990) conclude that aligned microfractures with foliation in mylonites remain open for effective pressures <50 MPa. Moreover, porosity in shear zone rocks can be as high as 8% (Géraud et al., 1995), and in addition to microfractures, porosity can be present in creep

cavities (Fusseis et al., 2009; Gilgannon et al., 2020; Menegon et al., 2015), grain boundaries (Kruhl et al., 2013; Mancktelow et al., 1998), or well-developed cleavage (Babuska & Cara, 1991; Kern & Wenk, 1990; Naus-Thijssen et al., 2011). With the FEM approach shown here, future studies could focus on characterizing the effect of real fracture networks, mineral phase, CPO, and microstructural arrangement data mapped from EBSD on the elastic anisotropic of shear zone rocks (Zhong et al., 2014).

Interpreting the difference between the porosity-free modeled rock elasticity and laboratory data as microfractures is an assumption in this study. It is possible that these differences are due to (Ji et al., 2003): (1) the elastic constants being representative of single crystals with no microfractures or imperfections that differ from the rock-forming minerals, (2) complex chemical compositions for the same single crystal that might change its elasticity, (3) representativeness of mineral volumes estimated from the EBSD sampled area of the whole rock, (4) type of averaging effective medium approach, and (5) mechanical interaction between minerals. In our study we avoid some of these potential biases by (1) analyzing with EBSD two thin sections from the top and bottom of the core covering most of the sample's cross section (Figure 2), (2) estimating the porosity-free velocities following a static and a dynamic wave propagation numerical approach (Figure 7), and (3) knowing that the dominant minerals (96%) in the protomylonite are commonly studied minerals: quartz, oligoclase plagioclase, and muscovite. Finally, the presence of microfractures in our rock is supported by imagining their existence and DEM modeling. It is possible however that part of the mismatch between the porosity-free and the experimental slow wave speeds is due to our assumption that micas are all aligned with foliation. Because we are unable to index these fine-grained micas using EBSD, all the nonindexed phases are assigned as muscovite with basal planes aligned to the foliation plane. Naus-Thijssen et al. (2011) show that wave speeds can vary significantly in the fast direction with varying mica orientations, but the slow wave speed is much less sensitive to mica alignment. Microphotographic and SEM analyses by Toy et al. (2008) and Dempsey et al. (2011) show that mica basal planes are aligned parallel to subparallel to foliation in Alpine Fault rocks. Therefore, the influence of slight mica misorientations on wave speeds does not seem critical to our interpretation.

Our experimental data generally correlate with previous laboratory studies by Okaya et al. (1995) and Christensen and Okaya (2007), but direct lithological comparison is not possible as the exact locations from which their samples were derived are unknown and microstructural images are absent in these studies. Extending core data to field has to be done carefully. Sun et al. (2012) highlight some differences in wave speeds and their pressure dependence for outcrop versus borehole core samples. The very high uplift and rapid erosion rates within the Alpine Fault Zone mean that our samples are essentially unweathered. The proposed remaining porosity in microfractures in the brittle crust of the Alpine Fault influence field measurements of seismic wave speeds and could have effects on the interpretation of electrical resistivity. They may also act as fluid pathways that contribute to the geodynamics and hydrogeology of the Alpine Fault. It is already acknowledged that the shallow, cataclastic part of the Alpine Fault Zone can act as a fluid barrier due to its low permeability (Sutherland et al., 2017), but little is known about the permeability of the hanging wall, where protomylonites are dominant. Mineral precipitation and dissolution can significantly alter the geophysical and fluid flow properties of rocks (Adam et al., 2013; Kanakiya et al., 2017; Williams et al., 2017), and future studies are certainly needed to better understand how these processes will impact the permeability structure of the zone (Zhong et al., 2017). We show that in addition to mineral phase, CPO, and microstructural arrangement, open grain boundaries and microfractures significantly influence seismic wave speeds throughout the Alpine Fault brittle zone. This can have significant implications for the interpretation and processing of seismic data at the Alpine Fault.

5. Implications of *P*-Wave Anisotropy for Imaging the Alpine Fault

Figure 10 is an idealized cross section of the Alpine Fault. It shows the listric nature of the fault, broad lithology definitions, and the best possible estimate of the location of the brittle-ductile transition. Active source field seismic experiments measure waves propagating at a range of angles to foliation: near-vertical to wide angles in reflection surveys and horizontal (parallel to foliation) in refraction surveys. Teleseismic waves are assumed to propagate near vertical to the Earth's surface. However, rock elastic anisotropy and the dip angle of the Alpine Fault plane make the analysis of raypath directions in such recordings nontrivial. Reflection seismic surveys to kilometers depth associated with DFDP (Feenstra et al., 2016; Lay et al., 2016), and

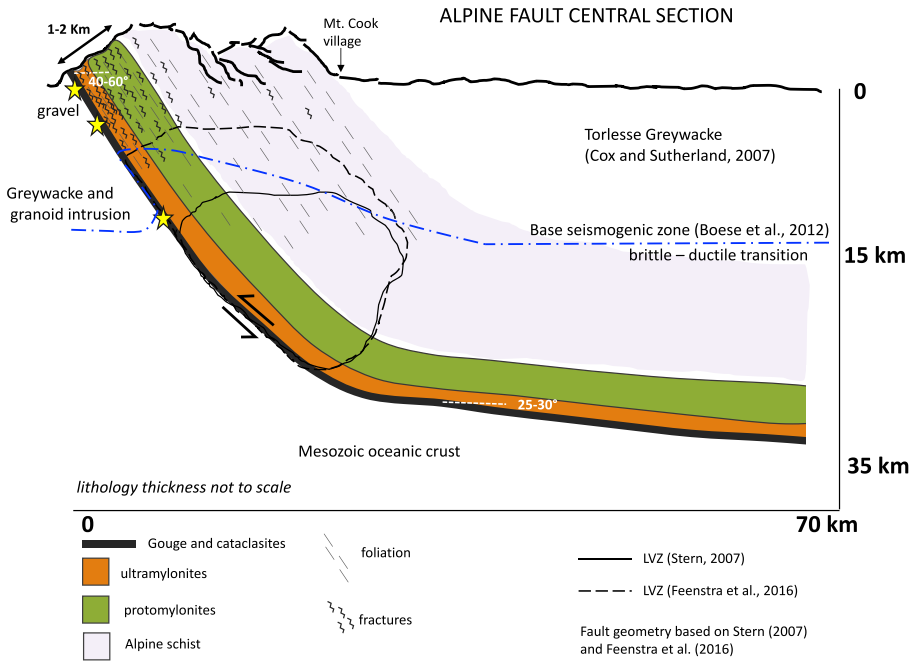

Figure 10. Alpine Fault cross section based on descriptions from Stern et al. (2007), Feenstra et al. (2016), Toy et al. (2008), Boese et al. (2012), Cox and Sutherland (2007), and references therein. Stars are approximate depths for which we perform anisotropic reflection coefficient modeling with angle of incidence.

larger-scale surveys undertaken during the SIGHT project (Stern et al., 2001, 2007) have focused on the central Alpine Fault.

Many shear zones show high seismic reflectivity (e.g., Fountain et al., 1984; Ji et al., 2003; Jones & Nur, 1982; Rey et al., 1994; Stern et al., 2007; Wang et al., 2005; Wenning et al., 2016). Jones and Nur (1982) measure mylonites, but due to their low volumes of micas, the resulting wave anisotropy and seismic reflectivity are low. Christensen and Szymanski (1988) measured a large range of micaceous quartzofeldspathic mylonitic gneisses and schist and show, based on synthetic seismograms, that seismic reflectivity increases with anisotropy. Rey et al. (1994) show that the reflectivity of a ductile shear zone depends on its thickness and anisotropy gradients, where the mylonitized zones are bounded by isotropic granite. The anisotropic gradients are associated to the volume and alignment of mica basal planes as a result of variable shear strain on the protolith. The mylonitized shear zones that result from nappe stacks in the Scandinavian Caledonides clearly play a role in seismic reflectivity, but such effect would be much less significant for the Alpine Fault shear zone as the protolith is a highly anisotropic schist (Christensen & Okaya, 2007; Simpson et al., 2020). In the studies mentioned above, high seismic reflectivity is suggested to be due to the highly anisotropic wave speeds of mylonitic shear zone rocks. However, most of these studies build on isotropic models with normal incidence reflectivity (Almqvist et al., 2013; Christensen & Szymanski, 1988; Fountain et al., 1984; Jones & Nur, 1982; Khazanehdari et al., 1998; Rey et al., 1994; Wang et al., 1989; Wenning et al., 2016) or acoustic impedance (Kern & Wenk, 1990) to explain the high reflectivity. Based on previously published experimental data, Khazanehdari et al. (1998) model reflectivity using the Zoepprietz and Knott equations as a function of incidence angle, but assume that the medium is isotropic. Barruol et al. (1992) present a 3-D ray tracing anisotropic model in a shear zone, but little interpretation on the seismic reflectivity is presented. Only recently, Simon et al. (2019) perform an anisotropic Kirchhoff prestack depth migration to improve seismic imaging of the Scandinavian Caledonides by taking into account the seismic anisotropy in the Seve Nappe Complex. To date, there is no quantitative interpretation of LVZs and high reflectivity at the Alpine Fault. We therefore model anisotropic reflectivity as a function of incidence angle based on our experimental data and literature values. We compare our experimental and numerical data to field observations aiming to answer if open grain boundaries and microfractures explain the LVZs and high seismic reflectivity of the Alpine Fault?

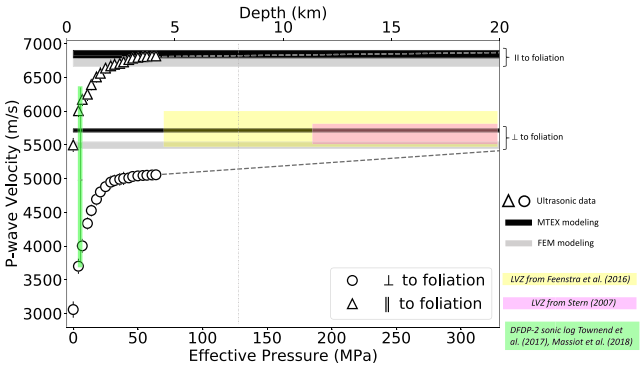

Figure 11. Ultrasonic *P*-wave velocity measurements under effective pressure (markers) extrapolated to greater effective pressures and compared to field observations. Black and gray bars are MTEX- and FEM-modeled wave speeds based on the EBSD data in Figure 3. Field observations are shown in colored boxes: *Green* is the sonic log wave speed recorded in the DFDP-2B well from Townend et al. (2017), *pink* is the low-velocity zone (LVZ) defined from teleseismic and refraction seismic analysis by Stern et al. (2007), and *yellow* is the LVZ defined by Feenstra et al. (2016) from microseismicity analysis on a 2 year dense seismic array in the central Alpine Fault. The dashed gray line is a visual extension of the experimental data as no model was fit to extend to effective pressures greater than 60 MPa.

5.1. LVZs at the Alpine Fault

Figure 11 compares our laboratory data to wave speed field observations. The effective pressure to depth correlation in this plot assumes fluids are at hydrostatic pressure. We believe such an assumption is valid as the hanging wall of the Alpine Fault has an active vertical groundwater flow (Coussens et al., 2018; Sutherland et al., 2017), which based on isotropic data can be present to depths of the brittle-ductile transition (Menzies et al., 2016). In Figure 11 we extrapolate, without assuming any model, the trend of the fast and slow *P*-wave velocities. We note that porosities below 0.5% and fractures with high aspect ratios probably still remain open throughout the brittle and seismogenic zone of the Alpine Fault (Boese et al., 2012).

Field seismic observations of LVZs are compiled and summarized in with our experimental and modeling data in Figure 11. Active and passive seismic surveys have identified LVZ above the Alpine Fault (Feenstra et al., 2016; Stern et al., 2007). The LVZ shows a drop in *P*-wave speeds by about 10% to 5,600 m/s with respect to the surrounding rocks (Figure 10). A shallow (1–3 km depth) LVZ has also been observed above the basement by Lay et al. (2016). The presence of fluids and high fluid pressures at great depths has been interpreted as the most probable cause for this LVZ and high seismic reflectivity (Feenstra et al., 2016; Stern et al., 2007), while anisotropy has mostly been thought to not be a significant contributor. The presence of fluids at depth has also been inferred to explain low resistivity values derived from magnetotelluric inversions (Wannamaker et al., 2002). Frost and Bucher (1994) also proposed that due to high thermal gradients associated with rapid uplift of the Alps, active metamorphic water may be trapped in grain boundaries in this region. Compared to dry fractures, fluids with microfractures stiffen their response to an applied stress (Nur & Simmons, 1969a). Therefore, identifying fractures in our sample supports the interpretations of fluid presence at the Alpine Fault Zone.

We compare our experimental and numerically simulated wave speeds at low effective pressures to the DFDP-2B borehole sonic log acquired in 2014 (Figure 11). The DFDP-2B well drilled to a depth of 818 m beneath the Whataroa Valley in the Central Southern Alps of New Zealand as part of the Deep Fault Drilling Project (Massiot et al., 2018; Townend et al., 2017; Toy et al., 2017). The sonic log records wave speeds at a range of angles to foliation (normal to foliation to 50° from normal) due to the high deviation of the DFDP-2B borehole. Nevertheless, there is a good correlation between the experimentally measured wave speed and the sonic log at the effective pressures (5.6–6.1 MPa) of the protomylonite interval encountered by DFDP-2B. The LVZ observations by Stern et al. (2007) and Feenstra et al. (2016) correlate with wave speeds representative of propagation normal to foliation, with little to no open fractures or grain boundaries as most of these depths are beneath the brittle-ductile transition (vertical dashed line in Figure 11). Wave speeds estimated from refraction surveys assume propagation parallel to the fault plane and thus foliation, while teleseismic data assume normal incidence to foliation (Stern et al., 2007). However, we cannot ignore the fact that due to the fault's listric nature and elastic wave anisotropy, it bends raypaths, and the measured wave speeds can depart from those assumed. It is the therefore possible that the LVZs observed at the Alpine Fault are partially the result of wave propagations normal or close to normal to foliation.

Finally, the shallow Alpine Fault Zone has a high geothermal gradient, and temperature could influence wave speeds. However, experimental studies on mylonites and phyllites show that as temperature increases to 700°C, velocities mostly remain unchanged in for some rocks could decrease by no more than 10%, while anisotropy remains close to constant with temperature (Kern et al., 2001; Kern & Wenk, 1990). We have not considered temperature into our study, and future studies involving temperature should consider the high geothermal gradient and active groundwater flow of the hanging wall of the Alpine Fault (Coussens et al., 2018; Sutherland et al., 2017). We now consider how anisotropy and open grain boundaries/fractures influence the high reflectivities that are inferred to be related to the Alpine Fault.

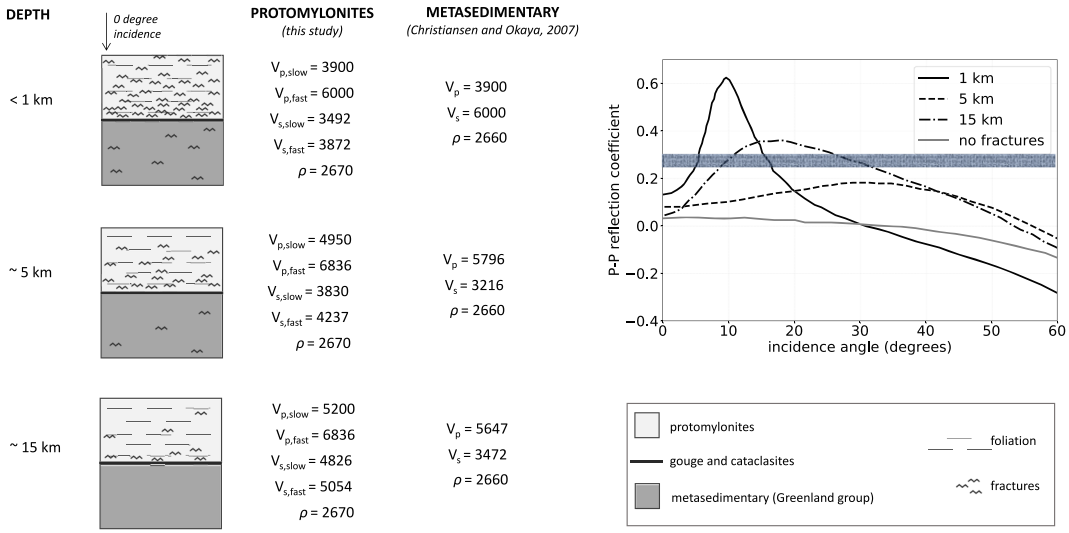

Figure 12. Exact vertical transversely isotropic (VTI) *P*-wave reflection coefficient as a function of incidence angle for three depth models at the Alpine Fault. VTI Protomylonites (data from this study) overlay isotropic metasedimentary rocks (data from Christensen and Okaya (2007)). The *no fractures* model refers to reflection coefficients for a porosity-free protomylonite with anisotropic wave speeds from MTEX/FEM. The horizontal gray bar represents the high reflective coefficients calculated at the fault plane by Stern et al. (2007).

5.2. High Seismic Reflectivity of the Alpine Fault Zone

Elastic wave anisotropy can significantly influence depth, amplitude, continuity, and focus of a seismic reflector (Simon et al., 2019; Tsvankin et al., 2010; Yan et al., 2004). The high elastic wave anisotropy of protoliths and mylonites at the Alpine Fault should be taken into account when processing and interpreting seismic data. Godfrey et al. (2002) discuss that the shallow highly dipping Alpine Fault plane, rock intrinsic anisotropy, and variable propagation raypath angles make the derivation of velocity models from forward modeling or travel time inversion challenging. That study also shows that when anisotropic processing is not applied to a seismic data set, the depth of a reflector (e.g., Alpine Fault trace) at 10 km can be overestimated by 10–15% for rocks with elastic wave anisotropy of 20%. However, the overestimation or underestimation of the depth of a seismic reflector would depend on the input velocities. At the spatial resolution of passive and active seismic data, the Alpine Fault's principal slip zone, cataclasites, and core damaged zone are below resolution. However, protomylonites within the Alpine Fault may be 300 to >500 m in thickness (Norris et al., 2007). As previously noted, this lithology and the Alpine schists are the most seismically anisotropic materials observed in the exhumed fault rock sequence, so it is reasonable to assume that they have the greatest effect on imaging the depth and structure of the fault.

Elastic wave anisotropy and the direction of the seismic wave ray to foliation can result in high reflection coefficients at the fault interface. Stern et al. (2007) estimated that the fault has a high reflection coefficient of 0.25–0.33 at 15–30 km in depth from SIGHT survey data. Lay et al. (2016) performed a tomographic inversion from the WhataDUSIE shallow seismic reflection survey (<5 km). They observe a strong reflector at depths between 1.5 and 2.2 km (but the reflection coefficient is not quantified) and a low-velocity layer at the top of the basement (0.8–2 km). They processed the data following an isotropic methodology but acknowledge that seismic anisotropy should be included in future seismic processing efforts. Future studies of seismic imaging at the Alpine Fault should focus on processing the data with the inclusion of seismic anisotropy (Simon et al., 2019; Tsvankin et al., 2010). Nonetheless, to show the effect of anisotropy and microfractures on seismic imaging of the Alpine Fault, we wrap up our study by performing a simple modeling of anisotropic reflection coefficients. These are studied with angle of incidence, and modeling is based on the laboratory and literature data and the geological model in Figure 12. So far we have discussed the lithologies of the fault's hanging wall. The lithologies across the Alpine Fault are asymmetric and the footwall of the shallow Alpine Fault has been mapped in the field as a metasedimentary rock. For the modeling of reflection coefficients, we use the full and exact solution of VTI anisotropic reflection coefficients (Daley & Hron, 1977)

and model the reflectivity with the TI Explorer from the Consortium for Research in Elastic Wave Exploration Seismology (CREWES). For the protomylonite layer, *S*-wave speeds are estimated from ultrasonic measurements on the protomylonite sample studied here, and we assume that the Thomsen parameter epsilon and delta are equal. The metasedimentary layer is assumed isotropic, and we use averaged experimental wave speeds from Christensen and Okaya (2007). Reflection coefficient as a function of angle show that for depths of 1, 5, and 15 km, the *P*-*P*-wave anisotropic reflection coefficient can reach 0.25. High reflectivity (>0.25) is observed for near incidence angle (<15°) for 5 km in depth or shallower. If fracture-free anisotropic protomylonites based on MTEX/FEM results are modeled, the reflection coefficient is no greater than 0.04 for all incidence angles. This means that to match the observed high reflectivities to these models, it is clear that open fractures have to be taken into account, not only at the microscale but also at the mesoscale. At mesoscales, Williams et al. (2017) observe open fractures subparallel to mylonitic foliation away from the fault damage zone (>160 m). Therefore, we can explain with rock physical properties at both microscales and mesoscales that the observed high reflection coefficients at the Alpine Fault can result from the presence of fractured, anisotropic rocks.

6. Conclusions

We have developed a multimethod approach to characterize the physical rock properties that control wave speeds and elastic anisotropy in the protomylonites that make up the bulk of New Zealand's Alpine Fault Zone. We have compared laboratory elastic wave speeds measured at various directions to foliation to porosity-free modeling of EBSD microstructural maps that contain information on CPO and texture of mineral phases. DEM and microimaging have been used to propose the existence of grain boundaries and fractures in this rock. These data have been used to model seismic signatures in the field to aid the interpretation of the LVZ and high seismic reflectivity at the Alpine Fault. We have found that

- Protomylonites can be described as having close to VTI symmetry by looking at laser-ultrasonic measurements and EBSD numerical modelings. Feldspar and quartz CPO contribute 2.36% and 0.74% to the total elastic wave anisotropy for PM-1 and PM-2 samples. However, the effective anisotropic symmetry of these minerals alone is not VTI.
- Dynamic FEM and effective medium estimates of porosity-free *P*-wave anisotropy agree at ∼20% for these samples once micas are included. However, absolute values of the fast and slow *P*-wave speeds calculated by MTEX are always higher than those from FEM. This can be due to the fact that MTEX averages the CPO of phases, losing the compositional layering information, while FEM preserves the latter in the modeling.
- The normal to foliation *P*-wave speed is slower than the porosity-free wave velocities modeled from EBSD data at effective pressures representative of the brittle regime in the Alpine Fault Zone. Ultrasonic velocity measurements sample microfractures and grain boundaries volumetrically within the rock. With the aid of DEM modeling and sCT and TEM imaging, we show the existence of open grain boundaries and microfractures. These have increasing aspect ratio and become larger contributions of fractures parallel to mica basal planes and thus foliation as effective pressures increase. Their presence explains the observation of lower wave speeds normal to foliation than the (porosity-free) MTEX/FEM-modeled values.
- The LVZ at the Alpine Fault spans the brittle and ductile regimes. Our laboratory and modeling conditions resemble the brittle regime. The LVZ for depths above 15 km can result from foliation normal propagation, without the need to invoke fractures. However, it is clear from the anisotropic high reflectivity modeling that partially open fractures or grain boundaries are required to retrieve the observed high seismic reflectivities at the fault and can also control LVZ shallower than 15 km. Using values of porosity-free anisotropic wave speeds in the reflectivity model does not result in the high reflectivity observed in the Alpine Fault. Therefore, to jointly interpret high seismic reflectivity and an LVZ, anisotropic and fractured protomylonites must be present.

Data Availability Statement

Sample OU86066 was collected by Katrina Sauer and is housed in the Otago University Geology Department Collections. Data and additional figures can be accessed at the University of Auckland figshare repository

(https://auckland.figshare.com/articles/Seismic_anisotropy_and_its_impact_on_imaging_the_Alpine_Fault_an_experimental_and_modeling_perspective/9974162).

Acknowledgments

We thank the Royal Society of New Zealand, Marsden Contract 14-UOA-028 for funding this research. The Avizo software and workstation employed were supported by the Royal Society of New Zealand Rutherford Discovery Fellowship (RDF) 16-UOO-1602 and a subcontract to GNS Science (GNS-MBIE00056) as part of the "Hikurangi subduction earthquakes and slip behaviour" MBIE Endeavour Project. Synchrotron and electron microscopic data acquisition was supported by RDF 16-UOO-1602 and SPring-8 Proposal No. 2017B1387 "How does particle arrangement in Fault Rocks affect the earthquakes they generate." We thank Kasper van Wijk for the help with Figure 1 and Jonathan Simpson and Jirapat Charoensawan for the help with the DEM code. We thank Tamara Jeppson and Cecile Massiot for providing the DFPD-2B sonic log and the DFDP-2B Science Team for their part in acquiring it. We thank the Consortium for Research in Elastic Wave Exploration Seismology (CREWES) for the use of the freely available TI Explorer. We greatly thank associate editor Dr. Almqvist for his suggestions to improve this manuscript.

References

Adam, L., Wijk, K., Otheim, T., & Batzle, M. (2013). Changes in elastic wave velocity and rock microstructure due to basalt-CO_2-water reactions. *Journal of Geophysical Research: Solid Earth*, *118*, 4039–4047. https://doi.org/10.1002/jgrb.50302

Allen, M. J., Tatham, D., Faulkner, D. R., Mariani, E., & Boulton, C. (2017). Permeability and seismic velocity and their anisotropy across the Alpine Fault, New Zealand: An insight from laboratory measurements on core from the Deep Fault Drilling Project phase 1 (DFDP-1). *Journal of Geophysical Research: Solid Earth*, *122*, 6160–6179. https://doi.org/10.1002/2017JB014355

Allmendinger, R. W., Sharp, J. W., Von Tish, D., Serpa, L., Brown, L., Kaufman, S., et al. (1983). Cenozoic and Mesozoic structure of the eastern Basin and Range province, Utah, from COCORP seismic-reflection data. *Geology*, *11*(9), 532–536.

Almqvist, B. S. G., Hirt, A. M., Herwegh, M., Ebert, A., Walter, J. M., Leiss, B., & Burlini, L. (2013). Seismic anisotropy in the Morcles nappe shear zone: Implications for seismic imaging of crustal scale shear zones. *Tectonophysics*, *603*, 162–178.

Almqvist, B. S. G., & Mainprice, D. (2017). Seismic properties and anisotropy of the continental crust: Predictions based on mineral texture and rock microstructure. *Reviews of Geophysics*, *55*, 367–433. https://doi.org/10.1002/2016RG000552

Babuska, V., & Cara, M. (1991). *Seismic anisotropy in the Earth* (Vol.10). Dordrecht, The Netherlands: Springer Science & Business Media.

Bachmann, F., Hielscher, R., & Schaeben, H. (2010). Texture analysis with MTEX—Free and open source software toolbox. *Solid State Phenomena*, *160*, 63–68.

Bachmann, F., Hielscher, R., & Schaeben, H. (2011). Grain detection from 2d and 3d EBSD data—Specification of the MTEX algorithm. *Ultramicroscopy*, *111*(12), 1720–1733.

Barruol, G., Mainprice, D., Kern, H., de Saint Blanquat, M., & Compte, P. (1992). 3D seismic study of a ductile shear zone from laboratory and petrofabric data (Saint Barthélémy Massif, Northern Pyrénées, France). *Terra Nova*, *4*(1), 63–76.

Batzle, M. L., Simmons, G., & Siegfried, R. W. (1980). Microcrack closure in rocks under stress: Direct observation. *Journal of Geophysical Research*, *85*(B12), 7072–7090.

Beck, C. (2009). Late Quaternary lacustrine paleo-seismic archives in north-western Alps: Examples of earthquake-origin assessment of sedimentary disturbances. *Earth-Science Reviews*, *96*(4), 327–344.

Ben-Zion, Y. (1998). Properties of seismic fault zone waves and their utility for imaging low-velocity structures. *Journal of Geophysical Research*, *103*(B6), 12,567–12,585.

Bestmann, M., & Prior, D. J. (2003). Intragranular dynamic recrystallization in naturally deformed calcite marble: Diffusion accommodated grain boundary sliding as a result of subgrain rotation recrystallization. *Journal of Structural Geology*, *25*(10), 1597–1613.

Birch, F. (1961). The velocity of compressional waves in rocks to 10 kilobars: 2. *Journal of Geophysical Research*, *66*(7), 2199–2224.

Blum, T. E., Adam, L., & van Wijk, K. (2013). Noncontacting benchtop measurements of the elastic properties of shales. *Geophysics*, *78*(3), C25–C31.

Boese, C. M., Townend, J., Smith, E., & Stern, T. (2012). Microseismicity and stress in the vicinity of the Alpine Fault, central Southern Alps, New Zealand. *Journal of Geophysical Research*, *117*, B02302. https://doi.org/10.1029/2011JB008460

Brace, W. F. (1965). Some new measurements of linear compressibility of rocks. *Journal of geophysical research*, *70*(2), 391–398.

Bruner, W. M. (1976). Comment on 'Seismic velocities in dry and saturated cracked solids' by Richard J. O'Connell and Bernard Budiansky. *Journal of Geophysical Research*, *81*(14), 2573–2576.

Burlini, L., & Kunze, K. (2000). Fabric and seismic properties of Carrara marble mylonite. *Physics and Chemistry of the Earth, Part A: Solid Earth and Geodesy*, *25*(2), 133–139.

Chiu, J. M., Johnston, A. C., & Yang, Y. T. (1992). Imaging the active faults of the central New Madrid seismic zone using PANDA array data. *Seismological Research Letters*, *63*(3), 375–393.

Cholach, P. Y., & Schmitt, D. R. (2006). Intrinsic elasticity of a textured transversely isotropic muscovite aggregate: Comparisons to the seismic anisotropy of schists and shales. *Journal of Geophysical Research*, *111*, B09410. https://doi.org/10.1029/2005JB004158

Christensen, N. I. (1965). Compressional wave velocities in metamorphic rocks at pressures to 10 kilobars. *Journal of Geophysical Research*, *70*(24), 6147–6164.

Christensen, N. I. (1989). Reflectivity and seismic properties of the deep continental crust. *Journal of Geophysical Research*, *94*(B12), 17,793–17,804.

Christensen, N. I., & Okaya, D. A. (2007). Compressional and shear wave velocities in South Island, New Zealand rocks and their application to the interpretation of seismological models of the New Zealand crust. *A Continental Plate Boundary: Tectonics at South Island, New Zealand*, *175*, 123–155.

Christensen, N. I., & Szymanski, D. L. (1988). Origin of reflections from the Brevard fault zone. *Journal of Geophysical Research*, *93*(B2), 1087–1102.

Coussens, J., Woodman, N., Upton, P., Menzies, C. D., Janku-Capova, L., Sutherland, R., & Teagle, D. A. H. (2018). The significance of heat transport by shallow fluid flow at an active plate boundary: The Southern Alps, New Zealand. *Geophysical Research Letters*, *45*, 10,323–10,331. https://doi.org/10.1029/2018GL078692

Cox, S. C., & Sutherland, R. (2007). Regional geological framework of South Island, New Zealand, and its significance for understanding the active plate boundary. *A Continental Plate Boundary: Tectonics at South Island, New Zealand*, *175*, 19–46.

Crampin, S. (1984). Effective anisotropic elastic constants for wave propagation through cracked solids. *Geophysical Journal International*, *76*(1), 135–145.

Daley, P. F., & Hron, F. (1977). Reflection and transmission coefficients for transversely isotropic media. *Bulletin of the Seismological Society of America*, *67*(3), 661–675.

Dempsey, E. D., Prior, D. J., Mariani, E., Toy, V. G., & Tatham, D. J. (2011). Mica-controlled anisotropy within mid-to-upper crustal mylonites: An EBSD study of mica fabrics in the Alpine Fault Zone, New Zealand. *Geological Society, London, Special Publications*, *360*(1), 33–47.

Eberhart-Phillips, D., & Bannister, S. (2002). Three-dimensional crustal structure in the Southern Alps region of New Zealand from inversion of local earthquake and active source data. *Journal of Geophysical Research*, *107*(B10), 2262. https://doi.org/10.1029/2001JB000567

Eberhart-Phillips, D., Han, D. H., & Zoback, M. D. (1989). Empirical relationships among seismic velocity, effective pressure, porosity, and clay content in sandstone. *Geophysics*, *54*(1), 82–89.

Eccles, J. D., Gulley, A. K., Malin, P. E., Boese, C. M., Townend, J., & Sutherland, R. (2015). Fault Zone Guided Wave generation on the locked, late interseismic Alpine fault, New Zealand. *Geophysical Research Letters*, *42*, 5736–5743. https://doi.org/10.1002/2015GL064208

Feenstra, J., Thurber, C., Townend, J., Roecker, S., Bannister, S., Boese, C., et al. (2016). Microseismicity and P–wave tomography of the central Alpine Fault, New Zealand. *New Zealand Journal of Geology and Geophysics*, *59*(4), 483–495.

Feng, R., & McEvilly, T. V. (1983). Interpretation of seismic reflection profiling data for the structure of the San Andreas fault zone. *Bulletin of the Seismological Society of America*, *73*(6A), 1701–1720.

Fountain, D. M., Hurich, C. A., & Smithson, S. B. (1984). Seismic reflectivity of mylonite zones in the crust. *Geology*, *12*(4), 195–198.

Frehner, M. (2013). Krauklis wave initiation in fluid-filled fractures by seismic body waves. *Geophysics*, *79*(1), T27–T35.

Frehner, M., & Schmalholz, S. M. (2010). Finite-element simulations of Stoneley guided-wave reflection and scattering at the tips of fluid-filled fractures. *Geophysics*, *75*(2), T23–T36.

Frehner, M., Schmalholz, S. M., Saenger, E. H., & Steeb, H. (2008). Comparison of finite difference and finite element methods for simulating two-dimensional scattering of elastic waves. *Physics of the Earth and Planetary Interiors*, *171*(1–4), 112–121.

Frost, B. R., & Bucher, K. (1994). Is water responsible for geophysical anomalies in the deep continental crust? A petrological perspective. *Tectonophysics*, *231*(4), 293–309.

Fusseis, F., Regenauer-Lieb, K., Liu, J., Hough, R. M., & De Carlo, F. (2009). Creep cavitation can establish a dynamic granular fluid pump in ductile shear zones. *Nature*, *459*(7249), 974–977.

Géraud, Y., Caron, J.-M., & Faure, P. (1995). Porosity network of a ductile shear zone. *Journal of Structural Geology*, *17*(12), 1757–1769.

Garboczi, E. J., Snyder, K. A., Douglas, J. F., & Thorpe, M. F. (1995). Geometrical percolation threshold of overlapping ellipsoids. *Physical Review E*, *52*(1), 819.

Gibson, R. G. (1998). Physical character and fluid-flow properties of sandstone-derived fault zones. *Geological Society, London, Special Publications*, *127*(1), 83–97.

Gilgannon, J., Poulet, T., Berger, A., Barnhoorn, A., & Herwegh, M. (2020). Dynamic recrystallisation can produce porosity in shear zones. *Geophysical Research Letters*, *47*, e2019GL086172. https://doi.org/10.1029/2019GL086172

Gillam, B. G., Little, T. A., Smith, E., & Toy, V. G. (2014). Reprint of Extensional shear band development on the outer margin of the Alpine mylonite zone, Tatare Stream, Southern Alps, New Zealand. *Journal of Structural Geology*, *64*, 115–134.

Godfrey, N. J., Christensen, N. I., & Okaya, D. A. (2002). The effect of crustal anisotropy on reflector depth and velocity determination from wide-angle seismic data: A synthetic example based on South Island, New Zealand. *Tectonophysics*, *355*(1–4), 145–161.

Gueguen, Y., & Dienes, J. (1989). Transport properties of rocks from statistics and percolation. *Mathematical Geology*, *21*(1), 1–13.

Gulley, A. K., Eccles, J. D., Kaipio, J. P., & Malin, P. E. (2017). The effect of gradational velocities and anisotropy on fault-zone trapped waves. *Geophysical Journal International*, *210*(2), 964–978.

Hole, J. A., Thybo, H., & Klemperer, S. L. (1996). Seismic reflections from the near-vertical San Andreas fault. *Geophysical Research Letters*, *23*, 237–240. https://doi.org/10.1029/96GL00019

Howarth, J. D., Fitzsimons, S. J., Norris, R. J., & Jacobsen, G. E. (2012). Lake sediments record cycles of sediment flux driven by large earthquakes on the Alpine fault, New Zealand. *Geology*, *40*(12), 1091–1094.

Ikari, M. J., Marone, C., & Saffer, D. M. (2011). On the relation between fault strength and frictional stability. *Geology*, *39*(1), 83–86.

Ivankina, T. I., Kern, H. M., & Nikitin, A. N. (2005). Directional dependence of P- and S-wave propagation and polarization in foliated rocks from the Kola superdeep well: Evidence from laboratory measurements and calculations based on TOF neutron diffraction. *Tectonophysics*, *407*(1–2), 25–42.

Ji, S., & Salisbury, M. H. (1993). Shear-wave velocities, anisotropy and splitting in high-grade mylonites. *Tectonophysics*, *221*(3–4), 453–473.

Ji, S., Saruwatari, K., Mainprice, D., Wirth, R., Xu, Z., & Xia, B. (2003). Microstructures, petrofabrics and seismic properties of ultra high-pressure eclogites from Sulu region, China: Implications for rheology of subducted continental crust and origin of mantle reflections. *Tectonophysics*, *370*(1–4), 49–76.

Ji, S., Wang, Q., Marcotte, D., Salisbury, M. H., & Xu, Z. (2007). P wave velocities, anisotropy and hysteresis in ultrahigh-pressure metamorphic rocks as a function of confining pressure. *Journal of Geophysical Research*, *112*, B09204. https://doi.org/10.1029/2006JB004867

Ji, S., Wang, Q., & Xia, B. (2003). P-wave velocities of polymineralic rocks: Comparison of theory and experiment and test of elastic mixture rules. *Tectonophysics*, *366*(3–4), 165–185.

Ji, S., Zhao, P., & Saruwatari, K. (1997). Fracturing of garnet crystals in anisotropic metamorphic rocks during uplift. *Journal of Structural Geology*, *19*(5), 603–620.

Johnson, J. L., tom Wörden, H., & van Wijk, K. (2014). PLACE: An Open-Source Python Package for Laboratory Automation, Control, and Experimentation. *Journal of Laboratory Automation*, *20*, 10–16. https://doi.org/10.1177/2211068214553022

Johnson, L. R., & Wenk, H.-R. (1974). Anisotropy of physical properties in metamorphic rocks. *Tectonophysics*, *23*(1–2), 79–98.

Jones, T., & Nur, A. (1982). Seismic velocity and anisotropy in mylonites and the reflectivity of deep crystal fault zones. *Geology*, *10*(5), 260–263.

Jones, T. D., & Nur, A. (1984). The nature of seismic reflections from deep crustal fault zones. *Journal of Geophysical Research*, *89*(B5), 3153–3171.

Kanakiya, S., Adam, L., Esteban, L., Rowe, M. C., & Shane, P. (2017). Dissolution and secondary mineral precipitation in basalts due to reactions with carbonic acid. *Journal of Geophysical Research: Solid Earth*, *122*, 4312–4327. https://doi.org/10.1002/2017JB014019

Karalliyadda, S. C., & Savage, M. K. (2013). Seismic anisotropy and lithospheric deformation of the plate-boundary zone in South Island, New Zealand: Inferences from local *S*-wave splitting. *Geophysical Journal International*, *193*, 507–530.

Kelly, C. M., Faulkner, D. R., & Rietbrock, A. (2017). Seismically invisible fault zones: Laboratory insights into imaging faults in anisotropic rocks. *Geophysical Research Letters*, *44*, 8205–8212. https://doi.org/10.1002/2017GL073726

Kern, H., Ivankina, T. I., Nikitin, A. N., Lokajíček, T., & Pros, Z. (2008). The effect of oriented microcracks and crystallographic and shape preferred orientation on bulk elastic anisotropy of a foliated biotite gneiss from Outokumpu. *Tectonophysics*, *457*(3–4), 143–149.

Kern, H., Popp, T., Gorbatsevich, F., Zharikov, A., Lobanov, K. V., & Smirnov, Y. P. (2001). Pressure and temperature dependence of V_P and V_S in rocks from the superdeep well and from surface analogues at Kola and the nature of velocity anisotropy. *Tectonophysics*, *338*(2), 113–134.

Kern, H., & Wenk, H.-R. (1990). Fabric-related velocity anisotropy and shear wave splitting in rocks from the Santa Rosa Mylonite Zone, California. *Journal of Geophysical Research*, *95*(B7), 11,213–11,223.

Khazanehdari, J., Rutter, E. H., Casey, M., & Burlini, L. (1998). The role of crystallographic fabric in the generation of seismic anisotropy and reflectivity of high strain zones in calcite rocks. *Journal of Structural Geology*, *20*(2–3), 293–299.

Kim, E., Kim, Y. H., & Mainprice, D. (2019). GassDem: A MATLAB program for modeling the anisotropic seismic properties of porous medium using differential effective medium theory and Gassmann's poroelastic relationship. *Computers and Geosciences*, *126*, 131–141. https://doi.org/10.1016/j.cageo.2019.02.008

Kruhl, J. H., Wirth, R., & Morales, L. F. G. (2013). Quartz grain boundaries as fluid pathways in metamorphic rocks. *Journal of Geophysical Research: Solid Earth*, *118*, 1957–1967. https://doi.org/10.1002/jgrb.50099

Langridge, R. M., Ries, W. F., Litchfield, N. J., Villamor, P., VanDissen, R. J., Barrell, D. J. A., et al. (2016). The New Zealand active faults database. *New Zealand Journal of Geology and Geophysics*, *59*(1), 86–96.

Lay, V., Buske, S., Lukács, A., Gorman, A. R., Bannister, S., & Schmitt, D. R. (2016). Advanced seismic imaging techniques characterize the Alpine Fault at Whataroa (New Zealand). *Journal of Geophysical Research: Solid Earth*, *121*, 8792–8812. https://doi.org/10.1002/2016JB013534

Leary, P. C., Li, Y. G., & Aki, K. (1987). Observation and modelling of fault-zone fracture seismic anisotropy—I. P, *SV* and *SH* travel times. *Geophysical Journal International*, *91*(2), 461–484.

Li, Y.-G., & Leary, P. C. (1990). Fault zone trapped seismic waves. *Bulletin of the Seismological Society of America*, *80*(5), 1245–1271.

Li, Y.-G., Leary, P., Aki, K., & Malin, P. (1990). Seismic trapped modes in the Oroville and San Andreas fault zones. *Science*, *249*(4970), 763–766.

Li, W., Schmitt, D. R., & Chen, X. (2020). Accounting for pressure-dependent ultrasonic beam skew in transversely isotropic rocks: Combining modelling and measurement of anisotropic wave speeds. *Geophysical Journal International*, *221*(1), 231–250.

Little, T. A., Holcombe, R. J., & Ilg, B. R. (2002). Kinematics of oblique collision and ramping inferred from microstructures and strain in middle crustal rocks, central Southern Alps, New Zealand. *Journal of Structural Geology*, *24*(1), 219–239.

Lloyd, G. E., Butler, R. W. H., Casey, M., & Mainprice, D. (2009). Mica, deformation fabrics and the seismic properties of the continental crust. *Earth and Planetary Science Letters*, *288*(1–2), 320–328.

Lokajíček, T., Kern, H., Svitek, T., & Ivankina, T. (2014). 3D velocity distribution of P- and S-waves in a biotite gneiss, measured in oil as the pressure medium: Comparison with velocity measurements in a multi-anvil pressure apparatus and with texture-based calculated data. *Physics of the Earth and Planetary Interiors*, *231*, 1–15.

Lokajíček, T., Svitek, T., Kern, H., & Wenk, H.-R. (2017). Rock elastic anisotropy study by X-ray synchrotron, neutron diffraction and ultrasonic methods. *Procedia Engineering*, *191*, 467–475.

Ma, K.-F., Tanaka, H., Song, S.-R., Wang, C.-Y., Hung, J.-H., Tsai, Y.-B., et al. (2006). Slip zone and energetics of a large earthquake from the Taiwan Chelungpu-fault Drilling Project. *Nature*, *444*(7118), 473.

Mainprice, D., Bachmann, F., Hielscher, R., Schaeben, H., & Lloyd, G. E. (2015). Calculating anisotropic piezoelectric properties from texture data using the MTEX open source package. *Geological Society, London, Special Publications*, *409*(1), 223–249.

Mainprice, D., & Nicolas, A. (1989). Development of shape and lattice preferred orientations: Application to the seismic anisotropy of the lower crust. *Journal of Structural Geology*, *11*(1–2), 175–189.

Mancktelow, N. S., Grujic, D., & Johnson, E. L. (1998). An SEM study of porosity and grain boundary microstructure in quartz mylonites, Simplon Fault Zone, Central Alps. *Contributions to Mineralogy and Petrology*, *131*(1), 71–85.

Massiot, C., Célérier, B., Doan, M.-L., Little, T. A., Townend, J., McNamara, D. D., et al. (2018). The Alpine Fault hangingwall viewed from within: Structural analysis of ultrasonic image logs in the DFDP-2B borehole, New Zealand. *Geochemistry, Geophysics, Geosystems*, *19*, 2492–2515. https://doi.org/10.1029/2017GC007368

Meléndez-Martínez, J., & Schmitt, D. R. (2016). A comparative study of the anisotropic dynamic and static elastic moduli of unconventional reservoir shales: Implication for geomechanical investigations. *Geophysics*, *81*(3), D245–D261.

Menegon, L., Fusseis, F., Stünitz, H., & Xiao, X. (2015). Creep cavitation bands control porosity and fluid flow in lower crustal shear zones. *Geology*, *43*(3), 227–230.

Menzies, C. D., Teagle, D. A. H., Niedermann, S., Cox, S. C., Craw, D., Zimmer, M., et al. (2016). The fluid budget of a continental plate boundary fault: Quantification from the Alpine Fault, New Zealand. *Earth and Planetary Science Letters*, *445*, 125–135.

Morales, L. F. G., Mainprice, D., & Kern, H. (2018). Olivine-antigorite orientation relationships: Microstructures, phase boundary misorientations and the effect of cracks in the seismic properties of serpentinites. *Tectonophysics*, *724*, 93–115.

Moyano, B., Spikes, K. T., Johansen, T. A., & Mondol, N. H. (2012). Modeling compaction effects on the elastic properties of clay-water composites. *Geophysics*, *77*(5), D171–D183.

Naus-Thijssen, F. M. J., Goupee, A. J., Johnson, S. E., Vel, S. S., & Gerbi, C. (2011). The influence of crenulation cleavage development on the bulk elastic and seismic properties of phyllosilicate-rich rocks. *Earth and Planetary Science Letters*, *311*(3–4), 212–224.

Naus-Thijssen, F. M. J., Goupee, A. J., Vel, S. S., & Johnson, S. E. (2011). The influence of microstructure on seismic wave speed anisotropy in the crust: Computational analysis of quartz-muscovite rocks. *Geophysical Journal International*, *185*(2), 609–621.

Niemeijer, A. R., & Spiers, C. J. (2005). Influence of phyllosilicates on fault strength in the brittle-ductile transition: Insights from rock analogue experiments. *Geological Society, London, Special Publications*, *245*(1), 303–327.

Norris, R. J., & Cooper, A. F. (1997). Erosional control on the structural evolution of a transpressional thrust complex on the Alpine Fault, New Zealand. *Journal of Structural Geology*, *19*(10), 1323–1342.

Norris, R. J., Cooper, A. F., Okaya, D., Stern, T., & Davey, F. (2007). The Alpine Fault, New Zealand: Surface geology and field relationships. *Geophysical Monograph-American Geophysical Union*, *175*, 159.

Nur, A., & Simmons, G. (1969a). The effect of saturation on velocity in low porosity rocks. *Earth and Planetary Science Letters*, *7*(2), 183–193.

Nur, A., & Simmons, G. (1969b). Stress-induced velocity anisotropy in rock: An experimental study. *Journal of Geophysical Research*, *74*(27), 6667–6674.

O'Connell, R. J., & Budiansky, B. (1974). Seismic velocities in dry and saturated cracked solids. *Journal of Geophysical Research*, *79*(35), 5412–5426.

Okaya, D., Christensen, N., Stanley, D., Stern, T., & Transect, S. I. G. (1995). Crustal anisotropy in the vicinity of the Alpine Fault zone, South Island, New Zealand. *New Zealand Journal of Geology and Geophysics*, *38*(4), 579–583.

Prior, D. J., Mariani, E., & Wheeler, J. (2009). EBSD in the earth sciences: Applications, common practice, and challenges. *Electron backscatter diffraction in materials science* (pp. 345–360). New York, USA: Springer.

Reches, Z., & Lockner, D. A. (1994). Nucleation and growth of faults in brittle rocks. *Journal of Geophysical Research*, *99*(B9), 18,159–18,173.

Rey, P. F., Fountain, D. M., & Clement, W. P. (1994). P wave velocity across a noncoaxial ductile shear zone and its associated strain gradient: Consequences for upper crustal reflectivity. *Journal of Geophysical Research*, *99*(B3), 4533–4548.

Sarout, J. (2012). Impact of pore space topology on permeability, cut-off frequencies and validity of wave propagation theories. *Geophysical Journal International*, *189*(1), 481–492.

Sarout, J., Cazes, E., Delle Piane, C., Arena, A., & Esteban, L. (2017). Stress-dependent permeability and wave dispersion in tight cracked rocks: Experimental validation of simple effective medium models. *Journal of Geophysical Research: Solid Earth*, *122*, 6180–6201. https://doi.org/10.1002/2017JB014147

Sayers, C. M., & Kachanov, M. (1995). Microcrack-induced elastic wave anisotropy of brittle rocks. *Journal of Geophysical Research*, *100*(B3), 4149–4156.

Schubnel, A., Benson, P. M., Thompson, B. D., Hazzard, J. F., & Young, R. P. (2006). Quantifying damage, saturation and anisotropy in cracked rocks by inverting elastic wave velocities. *Rock damage and fluid transport, part I* (pp. 947–973). Basel, Switzerland: Springer.

Schubnel, A., & Guéguen, Y. (2003). Dispersion and anisotropy of elastic waves in cracked rocks. *Journal of Geophysical Research*, *108*.

Shao, T., Ji, S., Oya, S., Michibayashi, K., & Wang, Q. (2016). Mica-dominated seismic properties of mid-crust beneath west Yunnan (China) and geodynamic implications. *Tectonophysics*, *677*, 324–338.

Shaocheng, J., Salisbury, M. H., & Hanmer, S. (1993). Petrofabric, P-wave anisotropy and seismic reflectivity of high-grade tectonites. *Tectonophysics*, *222*(2), 195–226.

Shapiro, S. A. (2003). Elastic piezosensitivity of porous and fractured rocks. *Geophysics*, *68*(2), 482–486.

Shigematsu, N., Prior, D. J., & Wheeler, J. (2006). First combined electron backscatter diffraction and transmission electron microscopy study of grain boundary structure of deformed quartzite. *Journal of Microscopy*, *224*(3), 306–321.

Simon, H., Buske, S., Hedin, P., Juhlin, C., Krauß, F., & Giese, R. (2019). Anisotropic Kirchhoff pre-stack depth migration at the COSC-1 borehole, central Sweden. *Geophysical Journal International*, *219*(1), 66–79.

Simpson, J., Adam, L., van Wijk, K., & Charoensawan, J. (2020). Constraining microfractures in foliated Alpine Fault rocks with laser ultrasonics. *Geophysical Research Letters*, *47*, e2020GL087378. https://doi.org/10.1029/2020GL087378

Simpson, J., van Wijk, K., Adam, L., & Smith, C. (2019). Laser ultrasonic measurements to estimate the elastic properties of rock samples under in situ conditions. *Review of Scientific Instruments*, *90*(11), 114,503.

Stern, T., Kleffmann, S., Okaya, D., Scherwath, M., & Bannister, S. (2001). Low seismic-wave speeds and enhanced fluid pressure beneath the Southern Alps of New Zealand. *Geology*, *29*(8), 679–682.

Stern, T., Okaya, D., Kleffmann, S., Scherwath, M., Henrys, S., & Davey, F. (2007). Geophysical exploration and dynamics of the Alpine fault zone. *A Continental Plate Boundary: Tectonics at South Island, New Zealand*, 207–233.

Sun, S., Ji, S., Wang, Q., Xu, Z., Salisbury, M., & Long, C. (2012). Seismic velocities and anisotropy of core samples from the Chinese Continental Scientific Drilling borehole in the Sulu UHP terrane, eastern China. *Journal of Geophysical Research*, *117*, B01206. https://doi.org/10.1029/2011JB008672

Sutherland, R., Eberhart-Phillips, D., Harris, R. A., Stern, T., Beavan, J., Ellis, S., et al. (2007). Do great earthquakes occur on the Alpine Fault in central South Island, New Zealand? *A Continental Plate Boundary: Tectonics at South Island, New Zealand*, *175*, 235–251.

Sutherland, R., Townend, J., Toy, V., & DFDP-2 Science Team (2015). Deep Fault Drilling Project (DFDP), Alpine fault boreholes DFDP-2A and DFDP-2B technical completion report, GNS Science report 2015/50.

Sutherland, R., Townend, J., Toy, V., Upton, P., Coussens, J., Allen, M., et al. (2017). Extreme hydrothermal conditions at an active plate-bounding fault. *Nature*, *546*(7656), 137.

Tobin, H. J., & Kinoshita, M. (2006). NanTroSEIZE: The IODP Nankai Trough seismogenic zone experiment. *Scientific Drilling*, *2*, 23–27.

Townend, J., Sutherland, R., & Toy, V. (2009). Deep Fault Drilling Project—Alpine Fault, New Zealand. *Scientific Drilling*, *8*, 75–82.

Townend, J., Sutherland, R., Toy, V. G., Doan, M.-L., Célérier, B., Massiot, C., et al. (2017). Petrophysical, geochemical, and hydrological evidence for extensive fracture-mediated fluid and heat transport in the Alpine Fault's hanging-wall damage zone. *Geochemistry, Geophysics, Geosystems*, *18*, 4709–4732. https://doi.org/10.1002/2017GC007202

Toy, V. G., Boulton, C. J., Sutherland, R., Townend, J., Norris, R. J., Little, T. A., et al. (2015). Fault rock lithologies and architecture of the central Alpine fault, New Zealand, revealed by DFDP-1 drilling. *Lithosphere*, *7*(2), 155–173.

Toy, V. G., Norris, R. J., Prior, D. J., Walrond, M., & Cooper, A. F. (2013). How do lineations reflect the strain history of transpressive shear zones? The example of the active Alpine Fault zone, New Zealand. *Journal of Structural Geology*, *50*, 187–198.

Toy, V. G., Prior, D. J., & Norris, R. J. (2008). Quartz fabrics in the Alpine Fault mylonites: Influence of pre-existing preferred orientations on fabric development during progressive uplift. *Journal of Structural Geology*, *30*(5), 602–621.

Toy, V. G., Prior, D. J., Norris, R. J., Cooper, A. F., & Walrond, M. (2012). Relationships between kinematic indicators and strain during syn-deformational exhumation of an oblique slip, transpressive, plate boundary shear zone: The Alpine Fault, New Zealand. *Earth and Planetary Science Letters*, *333*, 282–292.

Toy, V. G., Sutherland, R., Townend, J., Allen, M. J., Becroft, L., Boles, A., et al. (2017). Bedrock geology of DFDP-2B, central Alpine Fault, New Zealand. *New Zealand Journal of Geology and Geophysics*, *60*(4), 497–518.

Tsuji, T., & Iturrino, G. J. (2008). Velocity-porosity relationships in oceanic basalt from eastern flank of the Juan de Fuca Ridge: The effect of crack closure on seismic velocity. *Exploration Geophysics*, *39*(1), 41–51.

Tsvankin, I., Gaiser, J., Grechka, V., Van Der Baan, M., & Thomsen, L. (2010). Seismic anisotropy in exploration and reservoir characterization: An overview. *Geophysics*, *75*(5), 75A15–75A29.

Wallace, R. E. (1981). Active faults, paleoseismology, and earthquake hazards in the western United States. *Earthquake Prediction: An International Review*, *4*, 209–216.

Walsh, J. B. (1965). The effect of cracks on the compressibility of rock. *Journal of Geophysical Research*, *70*(2), 381–389.

Wang, Q., Ji, S., Salisbury, M. H., Xia, B., Pan, M., & Xu, Z. (2005). Pressure dependence and anisotropy of P-wave velocities in ultrahigh-pressure metamorphic rocks from the Dabie–Sulu orogenic belt (China): Implications for seismic properties of subducted slabs and origin of mantle reflections. *Tectonophysics*, *398*(1–2), 67–99.

Wang, C.-Y., Okaya, D. A., Ruppert, C., Davis, G. A., Guo, T.-S., Zhong, Z., & Wenk, H.-R. (1989). Seismic reflectivity of the Whipple Mountain shear zone in southern California. *Journal of Geophysical Research*, *94*(B3), 2989–3005.

Wannamaker, P. E., Jiracek, G. R., Stodt, J. A., Caldwell, T. G., Gonzalez, V. M., McKnight, J. D., & Porter, A. D. (2002). Fluid generation and pathways beneath an active compressional orogen, the New Zealand Southern Alps, inferred from magnetotelluric data. *Journal of Geophysical Research*, *107*(B6). https://doi.org/10.1029/2001JB000186

Wenning, Q. C., Almqvist, B. S. G., Hedin, P., & Zappone, A. (2016). Seismic anisotropy in mid to lower orogenic crust: Insights from laboratory measurements of V_p and V_s in drill core from central Scandinavian Caledonides. *Tectonophysics*, *692*, 14–28.

Williams, J. N., Toy, V. G., Smith, S. A. F., & Boulton, C. (2017). Fracturing, fluid-rock interaction and mineralisation during the seismic cycle along the Alpine Fault. *Journal of Structural Geology*, *103*, 151–166.

Wirth, R. (2004). Focused Ion Beam (FIB): A novel technology for advanced application of micro- and nanoanalysis in geosciences and applied mineralogy. *European Journal of Mineralogy*, *16*(6), 863–876.

Yan, L., Lines, L. R., & Lawton, D. C. (2004). Influence of seismic anisotropy on prestack depth migration. *The Leading Edge*, *23*(1), 30–36.

Zhao, W., Nelson, K. D., Che, J., Quo, J., Lu, D., Wu, C., & Liu, X. (1993). Deep seismic reflection evidence for continental underthrusting beneath southern Tibet. *Nature*, *366*(6455), 557.

Zhong, X., Frehner, M., Kunze, K., & Zappone, A. (2014). A novel EBSD-based finite-element wave propagation model for investigating seismic anisotropy: Application to Finero Peridotite, Ivrea-Verbano Zone, Northern Italy. *Geophysical Research Letters*, *41*, 7105–7114. https://doi.org/10.1002/2014GL060490

Zhong, X., Vrijmoed, J., Moulas, E., & Tajčmanová, L. (2017). A coupled model for intragranular deformation and chemical diffusion. *Earth and Planetary Science Letters*, *474*, 387–396.

Zoback, M., Hickman, S., & Ellsworth, W. (2010). Scientific drilling into the San Andreas fault zone. *Eos, Transactions American Geophysical Union*, *91*(22), 197–199.